



저작자표시-동일조건변경허락 2.0 대한민국

이용자는 아래의 조건을 따르는 경우에 한하여 자유롭게

- 이 저작물을 복제, 배포, 전송, 전시, 공연 및 방송할 수 있습니다.
- 이차적 저작물을 작성할 수 있습니다.
- 이 저작물을 영리 목적으로 이용할 수 있습니다.

다음과 같은 조건을 따라야 합니다:



저작자표시. 귀하는 원저작자를 표시하여야 합니다.



동일조건변경허락. 귀하가 이 저작물을 개작, 변형 또는 가공했을 경우에는, 이 저작물과 동일한 이용허락조건하에서만 배포할 수 있습니다.

- 귀하는, 이 저작물의 재이용이나 배포의 경우, 이 저작물에 적용된 이용허락조건을 명확하게 나타내어야 합니다.
- 저작권자로부터 별도의 허가를 받으면 이러한 조건들은 적용되지 않습니다.

저작권법에 따른 이용자의 권리는 위의 내용에 의하여 영향을 받지 않습니다.

이것은 [이용허락규약\(Legal Code\)](#)을 이해하기 쉽게 요약한 것입니다.

[Disclaimer](#)

공학박사 학위논문

**Study on surface defects for
InSb mid-IR FPAs**

InSb 중적외선 검출소자 개발을 위한
표면 결함 연구

2014년 8월

서울대학교 대학원

재료공학부

석철균

Abstract

Study on surface defects for InSb mid-IR FPAs

Chulkyun Seok

Department of Materials Science and Engineering

College of Engineering

Seoul National University

Indium-antimonide (InSb) is the most narrow band-gap material among III-V compound semiconductors. It has a high potential for device applications involving infrared detectors, high frequency electronics, and magnetic field sensors. In order to fabricate InSb devices with high performance, reducing dark current is the most important issue. The reduction of dark current has a great importance because it has strong relation with the detectivity of InSb photodiodes. Especially, InSb has a very weak atomic binding between In and Sb atom, surface defects can be easily generated by plasma energy and heat. These process-induced surface defects can act as surface trap sites in the energy bandgap and it is one of the main causes increasing the dark current. In this sense, to develop the InSb FPAs with minimized surface defects, it has to be explained what kind of surface defect can be generated by plasma or

thermal energy at the each step during the fabrication process and what kind of factors can affect the generation.

The objective of this thesis is to suggest the answers to the questions about both “What kind of defect can be generated by plasma and heat” and “How to reduce or prevent it”. To achieve this objective, the research has been focused on ‘how to measure the surface defect for investigating what kind of defect are existing’ and on ‘how to reduce and prevent the defect generation during fabrication process.

First, by applying Raman method to plasma-induced defect analysis, it was proved that the enhancement of TO scattering was originated from plasma-induced defects. As the applied RF power in Ar-ion etching raising from 50 to 200 W, the integrated area ratio of the TO mode to that of the LO mode (I_{TO}/I_{LO}) increased from 0.05 to 0.23 and the intensity of the TO phonon mode was fully restored back after annealing process under Sb ambient in the spectra. It clearly indicated that the origin of unintended enhancement of TO scattering in Raman spectra is plasma-induced defect due to the preferential loss of Sb atoms near the surface, not rough surface as reported by *F. Frost et al.*

Second, with increasing the environmental temperature from 25 to 500°C, phase change of indium-antimonide near the surface during annealing process were investigated by *in-situ* Raman spectroscopy. When the external temperature was above 450°C, elemental antimony phase began to form near the interface between thin native oxide and InSb substrate. Furthermore collecting spectral data with spatial resolution and encoding it in a 2D plot generates images with information complementary to optical imaging. As a result, images of

Raman map measured at 450, 475 and 500°C for Sb phonon (E_g) mode represented clearly the visible growth step of Sb region on the surface.

In a series of fabrication process, InSb surface is exposed to the applied plasma and heat frequently. We have developed the multi-step plasma etching to reduce the plasma-induced defects. As gradually increasing the amount of N_2 gas flow during the etching process, the smooth surface was obtained. Furthermore, Raman analysis of the InSb surface after the plasma etching indicated clearly that the multi-step etching process was an effective approach in reducing the plasma-induced defects on the surface.

Moreover, we have clarified the degradation mechanism of passivation properties and suggested the critical temperature to avoid it. The shape of C-V characteristics was dramatically changed when the deposition temperature was higher than 300°C. Raman spectra represented that elemental Sb accumulation resulted from the chemical reaction of Sb oxide with InSb substrate was responsible for the failure in the C-V characteristics of MIS structure. Thus, it was proved that the temperature have to be kept below 250°C during passivation process.

In conclusion, all of these works were aimed to enhance the device properties of InSb devices. Surface defects induced by plasma and thermal energy can cause the degradation of device performance. In this thesis, it was proven that Raman spectroscopy can analyze the change of surface structure very effectively. Furthermore, based on these results, we could reduce the dark current and enhance the R_0A effectively.

Keywords:

Indium-antimonide (InSb), Infrared (IR) detector, Dark current, Surface defects, Raman spectroscopy, Plasma-induced defects, Antimony (Sb) segregation

Student Number: 2008-20652

Contents

Abstract	i
Contents.....	v
List of Tables	viii
List of Figures	ix
Chapter 1 Introduction	1
1.1 InSb Focal Plane arrays (FPAs)	1
1.2 Photon Detection.....	2
1.2.1 Detectivity (D^*)	3
1.2.2 Dark current mechanism	4
1.3 Surface Defects Affecting Dark Current	10
1.3.1 Plasma-induced defects.....	10
1.3.2 Segregated antimony (Sb).....	11
1.4 Objective of the Thesis	12
1.5 Organization of the Thesis	13
1.6 References	14
Chapter 2 Experimental Details	16
2.1 Fabrication Equipments	16
2.1.1 Reactive Ion-beam Etcher (RIE).....	16
2.1.2 Plasma-enhanced Chemical Vapor Deposition (PECVD)...	16
2.1.3 E-gun Evaporator	16

2.1.4	Rapid Thermal Annealing (RTA)	17
2.2	Analysis Tools	17
2.2.1	Atomic force microscopy (AFM)	17
2.2.2	Field emission scanning electron microscopy (FE-SEM)...	18
2.2.3	Raman spectroscopy	18
2.2.4	Auger electron spectroscopy (AES).....	18
2.2.5	Capacitance-Voltage (C-V) measurement.....	19
2.3	Fabrication Procedure of InSb Sensor array	22
 Chapter 3 Plasma-induced surface defects.....		24
3.1	Motivation for defect analysis study	24
3.2	Raman Selection Rules	25
3.3	RF power dependence on forbidden TO phonon	30
3.4	Origin of TO scattering enhancement	40
3.4.1	Existing hypothesis	40
3.4.2	Defects related with preferential loss of Sb	41
3.5	Summary	47
3.6	References	48
 Chapter 4 Antimony (Sb) segregation.....		50
4.1	Motivation for thermal reaction study	50
4.2	In-situ analysis of Sb segregation	51
4.2.1	<i>In-situ</i> monitoring of Sb segregation	51
4.2.2	Chemical reaction on the surface	58
4.3	Temperature and Time dependence on Sb segregation	61
4.4	Summary	65

4.5	References	66
Chapter 5 Reduction of process-induced defect.....		68
5.1	Plasma etching for InSb FPAs.....	68
5.1.1	Comparison of conventional etching methods.....	68
5.1.2	Multi-step plasma etching (MSE) process	74
5.2	Growth Temperature Affecting Passivation	81
5.2.1	Temperature dependence on trap density.....	81
5.2.2	Failure cause of C-V characteristics	85
5.3	Summary	90
5.4	References	91
Chapter 6 Conclusion		93
6.1	Summary of results	93
6.2	Detectivity enhancement	96
Appendix A. Growth and Coalescence of InSb NCs.....		97
국 문 초 록.....		117
List of Publication		120
감사의 글.....		130

List of Tables

Table 3-1	Raman scattering tensors for a zinc-blende crystal	27
Table 3-2	Calculated intensity of TO, LO modes in backscattering configurations	31
Table 3-3	Selection Rules for Zinc-blende materials on (100) surfaces.	32
Table 3-4	Refractive index of 514 nm laser of InSb.	43
Table 5-1	Comparison of etching properties of MSE with IBE.....	80

List of Figures

Fig.1-1. Schematic image of InSb FPAs with hybrid architecture.	6
Fig.1-2. Schematic illustrations of (a) an InSb detector and (b) a band diagram for a p-n junction IR photodiode..	7
Fig.1-3. I-V characteristics of p-n diode in the dark and under illumination...	8
Fig.1-4. Dark current generation mechanism in a reverse biased p-n junction..	9
Fig.2-1. Images of Raman spectroscope (a) and heating cell (b).	20
Fig.2-2. Metal-Insulator-Semiconductor (MIS) structure for C-V measurement. 21	21
Fig.2-3. Schematic illustration of process flow for InSb photodiode: (1) p-InSb growth on n-InSb by using MOCVD, (2) Mesa-ething by using RIE, (3) SiO ₂ passivation by PECVD, and (4) Metal deposition by E-gun evaporator.....	23
Fig.3-1. (a) Notation of x-, y-, and z-directions for calculation of Raman selection rule and (b) schematic of vibration direction of longitudinal optical (LO) and transverse optical (TO) phonon...	29
Fig.3-2. Raman spectra of Ar ion beam etched InSb surfaces with different RF power.	36
Fig.3-3. (a) Fitting curves for the Raman spectrum of the InSb etched at 50 W and (b) Fitting curves for the Raman spectrum of the InSb etched at 200 W. Each Lorentzian curve represents TO and LO peak, respectively..	37
Fig.3-4. FWHM of LO peak (191 cm ⁻¹) and integrated area ratio of TO peak and LO peak as a function of RF power.	38
Fig.3-5. Polarized Raman spectra of Ar-ion beam etched InSb(100) surfaces (a) x(y'z')x ⁻ direction and (b) x(y'y')x ⁻ direction, respectively.....	39
Fig.3-6. Propagation of incident light at flat surface and rough surface.	43
Fig.3-7. Atomic Force Microscope (AFM) images of Ar ion beam etched InSb	

surfaces with different RF power.....	44
Fig.3-8. Relationship between surface roughness and TO phonon enhancement.	
45	
Fig.3-9. Raman spectra of the as-etched InSb(100) and damage-annealed InSb(100).....	46
Fig.4-1. <i>In-situ</i> Raman spectra of InSb(100) surfaces with increasing temperature.	55
Fig.4-2. Comparison of surface properties before and after annealing process. (a) comparison of Raman spectra and (b, c) comparison of AFM images.....	56
Fig.4-3. Optical microscopy images and 2-D Raman map images of InSb surfaces measured at 450, 475 and 500oC. Optical microscope images of annealed InSb surface observed at (a) 450, (b) 475 and (c) 500oC. 2-D Raman map of the spectrum integrated between 140 and 160 cm ⁻¹ , which can be assigned to the E _g phonon in elemental antimony(Sb) obtained at (d) 450, (e) 475 and (f) 500oC.	
57	
Fig.4-4. Composition profile of InSb surface (a) before and (b) after annealing process analyzed by AES. Ar-ion sputtering rate is about 1 – 1.5 nm/min.....	60
Fig.4-5. Raman spectra of RTA-annealed InSb(100) surfaces for 2.5 minutes with increasing temperature.....	62
Fig.4-6. Raman spectra of RTA-annealed InSb(100) surfaces at 300oC with increasing time.....	63
Fig.4-7. Raman spectra of long time-annealed InSb(100) surfaces	64
Fig.5-1. AFM images of plasma-etched InSb surfaces using (a) CH ₄ /H ₂ /Ar RIE, (b) Cl ₂ /Ar RIE, (c) Ar IBE, and (d) N ₂ RIE..	71
Fig.5-2. AFM images of plasma-etched InSb surfaces using Ar IBE and N ₂ RIE as increasing RF power. (a), (b), (c) and (d) show the etched	

surface using Ar IBE at 50, 100, 150 and 200 W, respectively. The etched surface using N ₂ RIBE at 50, 100, 150 and 200 W are shown in (e), (f), (g) and (h), respectively..	72
Fig.5-3. Etch rate and surface roughness as a function of RF power.	73
Fig.5-4. Process flow of multi-step etching process.	76
Fig.5-5. Surface morphology change during MSE process.	77
Fig.5-6. Etch rate and RMS roughness change during MSE process.	78
Fig.5-7. Comparison of Raman spectrum obtained from etched surface using MSE with Ar IBE.	79
Fig.5-8. C-V characteristics of Au/SiO ₂ /InSb MOS structures at frequency of 1 MHz.	83
Fig.5-9. Change of bulk trap density and interface trap density as a function of deposition temperature.	84
Fig.5-10. Raman spectra for the SiO ₂ /InSb samples deposited at various temperature.	87
Fig.5-11. Raman spectra of the sample deposited at 300°C and 350°C.	88
Fig.5-12. Band diagram of (a) MIS structure: Ti/SiO ₂ /InSb and (b) MIM structure: Ti/SiO ₂ /Sb/InSb.	89
Fig.A-1. (a) Schematic of MOCVD equipment and (b) process flow of InSb NCs epitaxial growth by using LP-MOCVD.	101
Fig.A-2. XRD results of epi-grown InSb NCs on GaAs (a) without elimination and (b) with elimination of background signals.	104
Fig.A-3. (a) Plane-view SEM image of InSb NCs. (b) Tilted-view SEM image of InSb NCs. (c) Cross-sectional SEM image of InSb NCs. (d) AFM image of InSb NCs.	105
Fig.A-4. Schematic explanation of catalyst-free grown InSb nano-crystal on GaAs substrate with facet index.	106
Fig.A-5. Plane-view SEM images of InSb NCs grown at 465oC using a	

Chapter 1.

Introduction

1.1 InSb Focal Plane Arrays (FPAs)

Indium antimonide (InSb) photodiodes have been available since the late 1950s. Its energy bandgap is about 0.23eV at 77 K (boiling temperature of liquid nitrogen), thus it is suitable materials for detecting infrared (IR) light. InSb technology is even more mature than HgCdTe (MCT) technology, because large size bulk substrates with good quality are commercially available.

One of the most important advances in IR technology is the development of 2-dimensional FPAs for use in the sensing arrays. InSb FPAs has been developed with the monolithic architecture as well as hybrid architecture. The monolithic architecture integrates all functions needed for solid-state imaging such as photon detection and electrical signal read-out. However, the best performance of InSb FPAs has been obtained from hybrid architecture. Figure 1-1 shows the architecture of InSb hybrid FPA. In this structure, the detection and readout parts of the device can be optimized separately,

so it can show enhanced performance in photon detection compare to monolithic architecture. [1]

1.2 Photon Detection

1.2.1 Detectivity (D^*)

For testing the IR FPAs, the performance characteristics of IR detectors should be measured. In this sense, detectivity (D^*) measurement has been widely used. [2-4]

Detectivity is expressed in unit $\text{cm.Hz}^{1/2}\text{W}^{-1}$, which recently is called “Jones”. The following equation for detectivity indicates the variables affecting the performance. [5]

$$D^* = \frac{\lambda}{hc} \eta q \left(\frac{4kT}{R_0A} + 2\eta q^2 Q_B \right)^{-\frac{1}{2}} \quad (1.1)$$

Where η is the quantum efficiency, A is the absorption area, Q_B is the background photon flux, and R_0A is the resistance at zero bias.

The term of $\frac{4kT}{R_0A}$ indicates the thermal noise in a detector itself and that of $2\eta q^2 Q_B$ indicates the background noise. In order to make the device having high performance, the term of thermal noise in

semiconductor have to be smaller than that of background noise, as shown (1.2). It is called background limited infrared photo-detector (BLIP) condition. [1]

$$\frac{4kT}{R_0 A} < 2\eta q^2 Q_B \quad (1.2)$$

The importance of Eq. (1.1) is that it represents the strong relation between $R_0 A$ and D^* . Detectivity is proportional to R_0 , resistance at zero bias, thus to enhance the detectivity of devices, R_0 should be increased. R_0 value can be calculated from the I-V characteristics of photodiode.

Figure 1-2 represents the schematic of an InSb photodiode (a) and band diagram (b). When the diode is exposed to the infrared light, electron-hole pair is generated in the depletion region. This photon-induced current is measured via integrated read out circuit (ROIC).

Figure 1-3 shows the I-V characteristics of InSb p-n photodiode in the dark and under illumination. The difference of current between dark and illuminated indicates the photocurrent. In this figure, the slope is the value of $\frac{I}{V}$, according to Ohm's law, it is the same value,

of $\frac{1}{R}$. In the Eq. (1-1), the value of R_0 is obtained from this term.

Thus, to obtain the maximized R_0 , the dark current I_0 should be minimized.

1.2.2 Dark current mechanism

In the previous section, the dark current affect the detectivity. Thus, to fabricate the device with high performance, the dark current generation should be suppressed. The dark current is the superposition of current contributions from three diode regions: bulk, depletion region, and surface.

Figure 1-4 represents some of the mechanisms by which dark current is generated in a reverse biased p-n junction [6]. The dark current is limited by three main mechanism, such as thermally generated current in the bulk and depletion region, tunneling or trap-assisted tunneling within depletion region, and surface leakage current. There are several mechanism to increase the surface leakage current. However, the most important mechanism is the surface generation current from surface states, so called Shockley-Read-Hall (SRH) mode.

In a real p-n junction, particularly in a narrow gap

semiconductor like InSb, the surface leakage current is strongly related with dark current. Furthermore, during the fabrication process, a number of surface defects can be generated.

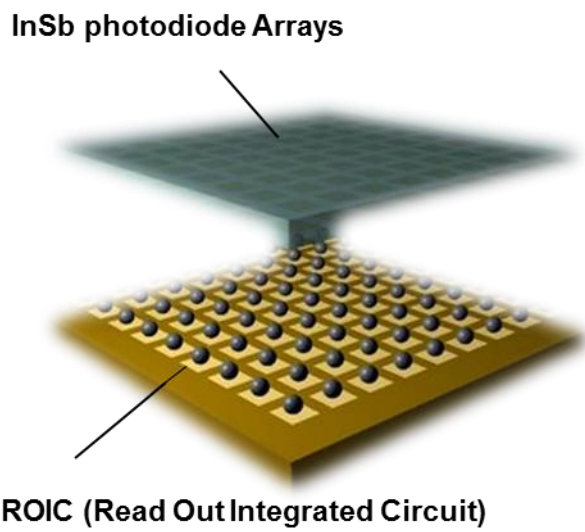


Fig.1-1. Schematic image of InSb FPAs with hybrid architecture.

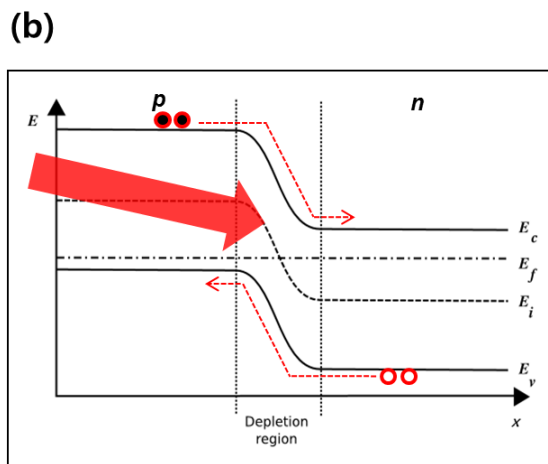
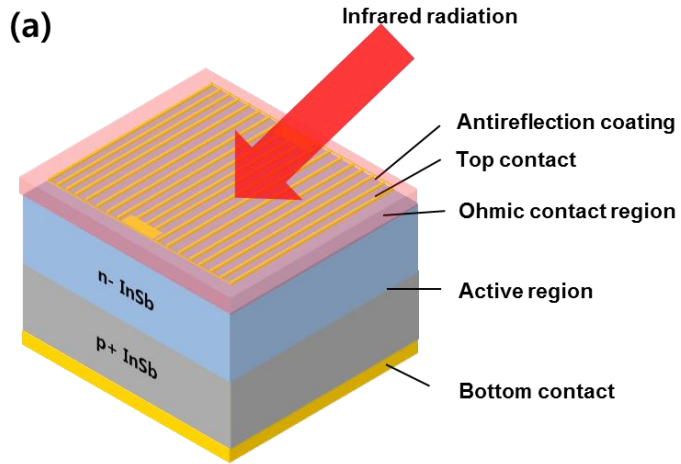


Fig.1-2. Schematic illustrations of (a) an InSb detector and (b) a band diagram for a p-n junction IR photodiode.

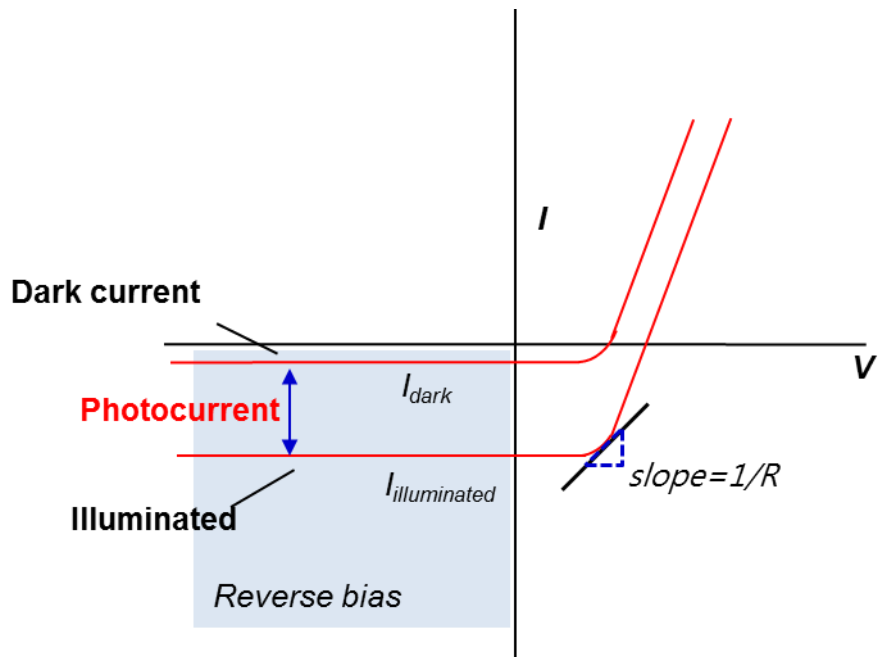


Fig.1-3. I-V characteristics of p-n diode in the dark and under illumination.

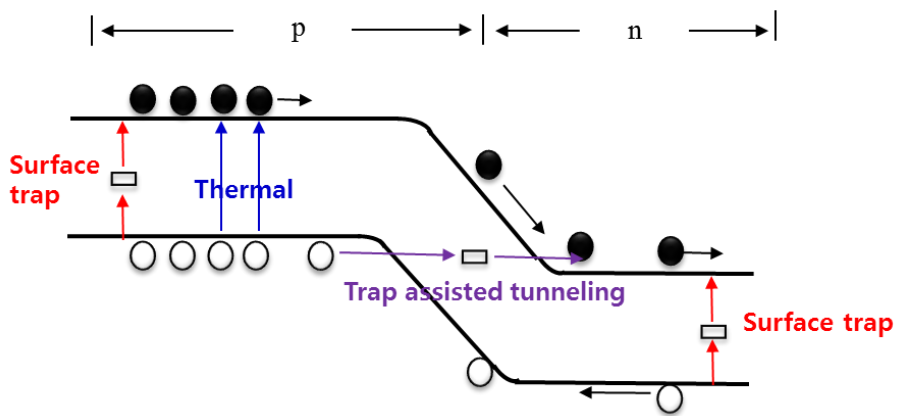


Fig.1-4. Dark current generation mechanism in a reverse biased p-n junction. [6]

1.3 Surface Defects Affecting Dark Current

1.3.1 Plasma-induced defect

In the section 1.2.2, the various sources contributing the dark current were discussed. Especially, in the case of InSb, the reduction of dark current is the most important issue. InSb has the narrowest band gap energy (0.18 eV at room temperature) and the highest electron mobility (80000 cm²/Vs) among the III-V compound semiconductors, for normal operation, thus InSb photodiodes have to put into the cooling system keeping the temperature around 77 K (boiling temperature of liquid nitrogen) because it can reduce the thermally generated current critically affecting the device performance. However, even in the cooling system with cryogenic temperature, the surface leakage current generated via trap site cannot be prevented. In this sense, the reduction of surface defect acting as a surface trap site has a great importance.

As discussed by *J. Sendra et al.*[7], Sb vacancies caused by preferential sputtering can account for the increase of the number of defects near the etched surface. It was also reported that plasma-induced point defects such as vacancy and interstitial atom can affect the electrical properties of InSb [10,11]. Because this type of defects can

make a deep level in the energy band, it is one of the main causes increasing the surface leakage current. Moreover, Sb vacancy can make the diffusion of impurity existing on the surface easily, and the diffused atom can degrade the electrical and optical properties of InSb devices. [12]

1.3.2 Segregated antimony (Sb)

Due to the low melting temperature (525°C) of InSb, antimony segregation can be occurred. As the excess antimony in bulk region can be a role of impurity and it causes to decrease of electron and hole mobility. [13] Furthermore, excess Sb existing near the surface can be a surface trap site increasing leakage current.

When the excess Sb atoms were segregated on the surface, it can make other problems. Due to the existing Sb thin layer between InSb and contact metal layer, the ohmic and nonohmic resistance can be changed. Moreover, the Sb atoms can diffuse into oxide and nitride passivation layer and act as an impurity, it cause the increasing bulk trap density. [14]

1.4 Objective of the Thesis

The reduction of dark current has a great importance because it has strong relation with the detectivity of InSb photodiodes. Especially, InSb has a very weak atomic binding between In and Sb atom, surface defects can be easily generated by plasma energy and heat. These process-induced surface defects can act as surface trap sites in the energy bandgap and it is one of the main causes increasing the dark current. In this sense, to develop the InSb FPAs with minimized surface defects, it has to be explained what kind of surface defect can be generated by plasma or thermal energy at the each step in the fabrication process and what kind of factors can affect the generation.

The objective of this thesis is to suggest the answers to the questions about both “What kind of defect can be generated by plasma and heat” and “How to reduce or prevent it”. To achieve this objective, the research has been focused in two ways. The first focus is on how to measure the surface defect for investigating what kind of defect are existing. It is difficult to study defect generation mechanism within a few nanometer thickness beneath the surface using conventional analysis tools. Therefore we have adopted new method to study surface defects by using Raman spectroscopy. Plasma-etched surfaces and annealed

surfaces have been studied and factors affecting the defect generation have also been investigated.

The second focus is on how to reduce and prevent the defect generation during fabrication process. In a series of fabrication process, InSb surface is exposed to the applied plasma and heat frequently. We have developed the multi-step plasma etching to reduce the plasma-induced defects. Moreover, we have clarified the degradation mechanism of passivation properties and suggested the critical temperature to avoid it.

1.5 Organization of the Thesis

There are six chapters in this thesis. Chapter 2 explains the experimental and analysis tools, including fabrication procedure of InSb photodiode. Chapter 3 and 4 discuss the results of surface defects on InSb study. Chapter 3 explain the plasma-induced surface defect via Raman spectroscopy and Chapter 4 explain the antimony segregation dependence on temperature and time. Chapter 5 describe the methods to reduce the surface defect during fabrication processing. Chapter 6 summarizes the results of this study and shows dark current reduction when applying the results of this study to InSb diodes.

1.6 References

- [1] A. Rogalski, *Infrared Detectors 2nd edition*, CRC Press, New York (2011).
- [2] R. D. Hudson, *Infrared System Engineering*, Wiley, New York, (1969).
- [3] W. I. Wolfe, and G. J. Zissis, *The Infrared Handbook*, Office of Naval Research, Washington DC (1985).
- [4] J. D. Vincent, *Fundamentals of Infrared Detector Operation and Testing*, Wiley, New York (1990).
- [5] R. C. Jones, *Performance of Detectors for Visible and Infrared Radiation*, Vol. **5**, Academic Press, New York (1952).
- [6] C. T. Elliot, N. T. Gordon, *Handbook on Semiconductors*, North-Holland, Amsterdam, **4**, 841-936 (1993).
- [7] J. R. Sendra, G. Armelles, T. Utzmeier, J. Anguita, and F. Briones, *J. Appl. Phys.* **79**, 8853 (1996).
- [8] J. Liu, and T. Zhang, *Appl. Surf. Sci.* **126**, 231-234 (1998).
- [9] F. H. Eisen, *Phys. Rev.* **123**, 736 (1961).
- [10] J. E. Greene, and C. E. Wickersham, *J. Appl. Phys.* **47**, 3630 (1976).
- [11] W. Hanus, and M. Oszwaldowski, *Thin Solid Films*, **61**, 235-239 (1979).
- [12] J. Goc, M. Oszwaldowski, and H. Szweycer, *Thin Solid Films*, **142**,

227-240 (1986).

[13] H. Okimura, Y. Koizumi, and S. Kaida, *Thin Solid Films*, **254**, 169-174 (1995).

[14] S. Mizuo, and H. Higuchi, *Jpn. J. Appl. Phys.*, **20**, 739 (1981).

Chapter 2.

Experimental Details

2.1 Fabrication Tools

2.1.1 Reactive Ion-beam Etcher (RIE)

Ion beam etching (IBE) was performed in an Oxford Instrument model RIE 80 plus system using Ar gas. The gas flow was adjusted to 30 sccm for Ar IBE and working pressure was set to 100 mTorr. The RF power was changed from 50 W to 200 W in order to investigate the RF power dependence on the generation of plasma-induced defect.

2.1.2 Plasma-enhanced chemical vapor deposition (PECVD)

SiO₂ thin films were deposited on InSb substrate to passivate the dangling bonds existing on the surface. Source gases used in experiments were SiH₄, N₂O and N₂. The RF power was set to 60 watts with 187 kHz. To study the effect of deposition temperature on interface and bulk trap density, it was controlled from 100 to 350 °C .

2.1.3 E-gun evaporator

Ti and Au thin film were deposited by using E-gun evaporator. The thickness of Ti and Au metal was 10 and 100 nm, respectively. To reduce the contact resistance, following annealing at 250°C for 2 min was conducted in RTA.

2.1.4 Rapid Thermal Annealing (RTA)

Annealing was conducted by using rapid thermal annealing (RTA) named KVT-3006T. The main chamber is connected with dry pump backed by rotary pump and the base pressure is less than 10^{-3} Torr. Main chamber consisted of heater and graphite susceptor. Ar was used as an ambient gas. Flow rate of Ar gas and working pressure are fixed at 100 sccm and 10 Torr, respectively. In order to investigate the surface reaction, the temperature and time were changed from 100 °C to 450°C and 2.5 minutes to 120 minutes, respectively.

2.2 Analysis Tools

2.2.1 Atomic force microscope (AFM)

Non-contact AFM measurements were performed in using Park systems XE-100 in order to investigate surface morphology. The Au-

coated Si tips were used. For statistical analyses, XEI ver. 1.8.0 was used.

2.2.2 Field emission scanning electron microscope (FE-SEM)

FE-SEM analyses were performed by using a SU-70 of Hitachi, which incorporates a cold field emission electron source and provides 1 nm microscope resolution at 10 kV, magnification range of 30 - 800,000x.

2.2.3 Raman spectroscopy

The Raman scattered light signal was dispersed by a Horiba Jobin-Yvon LabRam HR spectrometer and detected with a liquid-nitrogen-cooled CCD detector. The 514.5 nm line of an Ar-ion laser was used as the excitation source. To examine the temperature dependence of Raman scattering of InSb surface, as shown in Figure 2-1, Linkham THMS 600 heating cell with 1°C temperature accuracy and stability was used. After reaching the highest temperature of 500 °C, the sample was cooled down to room temperature. This Raman analysis was performed in collaboration with Prof. In-Sang Yang's laboratory in Ewha Womans University.

2.2.4 Auger electron spectroscopy (AES)

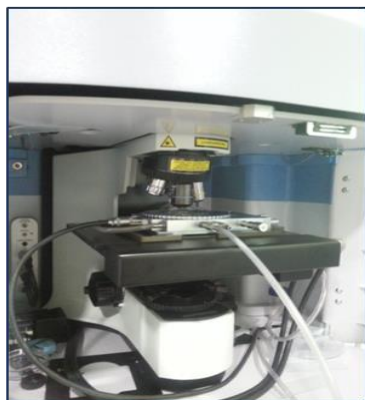
Atomic concentration of In, Sb, O, C were measured by a PHI-700 made by ULVAC-PHI in KIST. To conduct depth-profile, Ar sputtering with sputter rate of 1 - 1.5 nm/min was used.

2.2.5 Capacitance-Voltage (C-V) measurement

C-V measurement was performed by Agilent 4980A at 77 K. 7 mm x 7 mm MIS samples were mounted on PCB and the bottom of the sample was attached by silver paste. Top contact was wired by Au wire and indium (In) was used as welding metal. Then, the sample was emerged in liquid nitrogen and C-V measurement was performed. Sweep rate was 0.1 V/sec.

Figure 2-2 represents the prepared sample with metal-insulator-semiconductor (MIS) structure for C-V measurement. SiO₂ was deposited by PECVD and Au/Ti metal was deposited by E-gun evaporator.

(a)



(b)

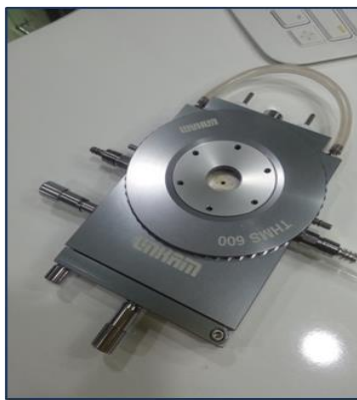


Fig.2-1. Images of Raman spectroscope (a) and heating cell (b).

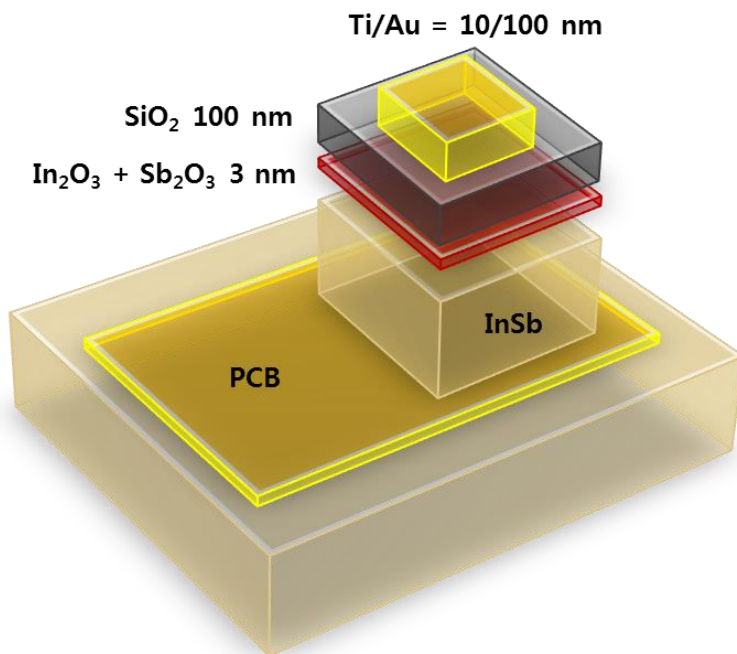


Fig.2-2. Metal-Insulator-Semiconductor (MIS) structure for C-V measurement.

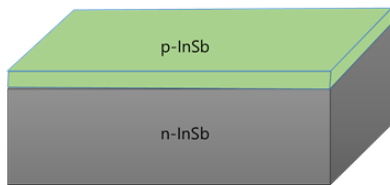
2.3 Fabrication procedure of InSb photodiode

Figure 2-3 shows the fabrication procedure of InSb photodiodes. In the first stage, Zn-doped InSb layer was epitaxially grown on Te-doped InSb(100) wafer by using MOCVD. The growth temperature was 500°C and working pressure is about 76 Torr. TMIIn and TMSb were used as a metal-organic sources. The flow rate of TMIIn and TMSb was 20 sccm and 9 sccm, respectively.

In the next stage, for obtaining mesa-structure with etch-depth of 1 μm , Ar ion beam etching was conducted by RIE. The flow rate of Ar gas was adjusted 30 sccm and the working pressure was fixed 100 mTorr.

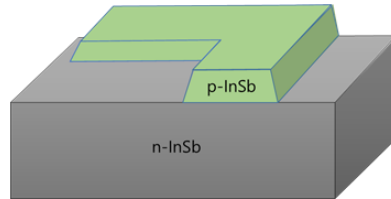
For surface passivation, SiO_2 was deposited by using PECVD. The thickness of SiO_2 was 100 nm. The deposition temperature was adjusted 250°C and RF power was fixed 60 W.

In the last stage, Ti/Au was deposited by using E-gun evaporator. The thickness of metal layer was 10 and 100 nm, respectively. Metal pad were patterned by lift-off process. Finally, deposited metal on InSb was annealed at 200°C for lowering the contact resistance.



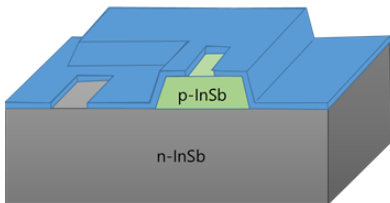
(1) Epitaxial growth

: MOCVD / 500°C



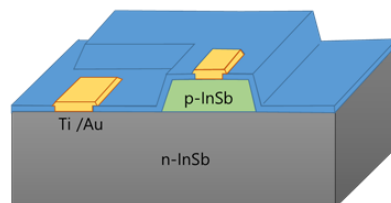
(2) Mesa-etching

: RIE / 25°C



(3) Passivation

: PECVD / 200°C



(4) Metal deposition

: E-gun evaporator / 25°C

+ RTA / 200°C

Fig.2-3 Schematic illustration of process flow for InSb photodiode: (1) p-InSb growth on n-InSb by using MOCVD, (2) Mesa-etching by using RIE, (3) SiO₂ passivation by PECVD, and (4) Metal deposition by E-gun evaporator.

Chapter 3.

Plasma-induced surface defects

3.1 Defect analysis via Raman spectroscopy

To make a device with epitaxially grown InSb layer, etching is one the essential step in the semiconductor fabrication process. However, due to the weak binding energy between In atom and Sb atom, InSb can be more easily damaged by bombarded ions during the process compared to other semiconductors. In this respect, a key requirement for InSb research and application is the ability to identify and characterize it, both at the lab- and at the mass-production scale. So far, the surface properties of InSb have been investigated using atomic force microscopy (AFM), scanning tunneling microscopy (STM), X-ray photoelectron spectroscopy (XPS) and electron energy loss spectroscopy (EELS). These investigations can reveal the change of surface morphology, the atomic reconstruction and the charge accumulation near the surface. To be appealing, a characterization tool must be nondestructive, fast, with high resolution and give the maximum structural and electronic information. However,

all of these methods are not enough to widely use and to evaluate the fine damaged structure induced by ion beam nondestructively, fast and directly. To overcome the limitation, resonant Raman spectroscopy which can satisfy all of these conditions was suggested as an alternative in this study.

Raman spectroscopy has been attracted a lot of attention and investigated actively in the fast growing field of graphene. Antimony also has a resonance property which is similar to graphene and the penetration depth of incident light source of Raman spectroscopy is about 8.9 nm in InSb crystal, thus Raman spectroscopy can examine the fine modification of InSb surface effectively. However, the effect of plasma-induced defect on Raman scattering have not been clearly explained yet. In this chapter, to study the plasma-induced defect affecting Raman scattering, by increasing the applied RF power from 50 to 200 W in Argon ion beam etching (IBE), the effect of plasma-induced surface damage on Raman spectrum of crystalline InSb was investigated.

3.2 Raman selection rule

Theoretically the Raman scattering has a strong relation to the geometry of a crystal, thus the difference in atomic arrangement can change the scattering modes. The intensities of Raman scattering can be calculated from the below equation:

$$I_s \propto |e_i \cdot R \cdot e_s|^2 \quad (3.1)$$

where \mathbf{R} is the Raman tensor which depends on the crystal symmetry and e_i and e_s are the polarization of the incident and scattered wave, respectively. InSb has a zinc-blende structure with a 0.648 nm lattice constant. The space group of InSb is $F\bar{4}3m$ and it belongs to the point group $F\bar{4}3m(T_d)$.⁵ Due to the symmetry, the following Raman tensors are considered.

$$R_x = \begin{pmatrix} 0 & 0 & 0 \\ 0 & 0 & d \\ 0 & d & 0 \end{pmatrix}, R_y = \begin{pmatrix} 0 & 0 & d \\ 0 & 0 & 0 \\ d & 0 & 0 \end{pmatrix}, R_z = \begin{pmatrix} 0 & d & 0 \\ d & 0 & 0 \\ 0 & 0 & 0 \end{pmatrix} \quad (3.2)$$

Where d is the one linearly independent component.

Table 3.1 represents the Raman scattering tensors for a zinc-blende crystal. The selection rules for Raman scattering in InSb for different scattering geometries can be determined by using these term.

System	Class	C_{6v}	Quadratic	Raman tensor
zinc-blende	$\bar{4}3m$ (T_d)	R(X)	$\sigma_{xx} + \sigma_{yy}, \sigma_{zz}$	$\mathbf{R(X)} = \begin{pmatrix} 0 & 0 & 0 \\ 0 & 0 & d \\ 0 & d & 0 \end{pmatrix}$
		R(Y)	$(\sigma_{xz}, \sigma_{yz})$	$\mathbf{R(Y)} = \begin{pmatrix} 0 & 0 & d \\ 0 & 0 & 0 \\ d & 0 & 0 \end{pmatrix}$
		R(Z)	$(\sigma_{xx} - \sigma_{yy}, \sigma_{xy})$	$\mathbf{R(Z)} = \begin{pmatrix} 0 & d & 0 \\ d & 0 & 0 \\ 0 & 0 & 0 \end{pmatrix}$

Table 3-1 Raman scattering tensors for a zinc-blende crystal.

Backscattering geometry is the geometry in which the directions of the incident and scattered photons are antiparallel to each other. Since this geometry is the one used in our experiments we will use it in our example.

Figure 3.1 (a) illustrates the x , y and z directions with respect to the sample geometry and Figure 3.1 (b) indicates the scattering direction of longitudinal optical (LO) and transverse optical (TO) phonon. In the notation of polarized Raman scattering, x, y, z, \bar{x}, y' and z' denote $[001], [100], [010], [00\bar{1}], [110]$ and $[\bar{1}\bar{1}0]$, respectively.

Table 3.2 gives selection rules for other backscattering geometries on the (100) surface of zinc-blende materials. In this table, we used the Porto's notation given by:

$$k_i(e_i, e_s)k_s$$

where k_i and k_s are the directions of the incident and scattered photons, respectively, and e_i and e_s are the polarizations of the incident and scattered photons, respectively. The Raman selection rules for backscattering geometries in zinc-blende-type crystals are summarized

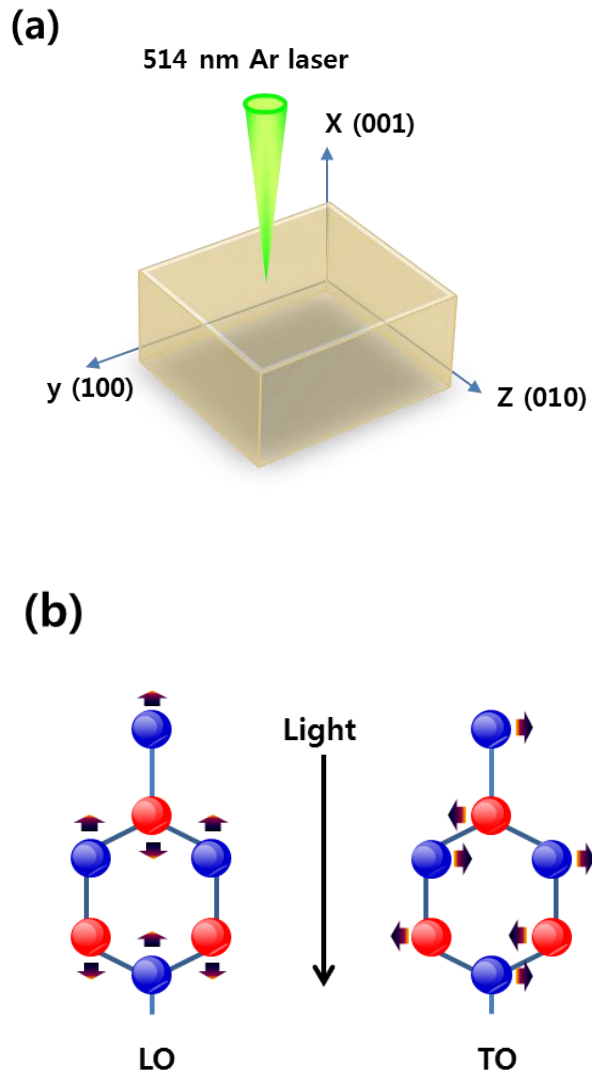


Fig. 3.1 (a) Notation of x-, y-, and z-directions for calculation of Raman selection rule and (b) schematic of vibration direction of longitudinal optical (LO) and transverse optical (TO) phonon.

in Table 3.3.

In the calculation of Raman selection rule for InSb with zinc-blende structure as shown in Table 3.3, LO phonon scattering is allowed in backscattering from the (100) surfaces while the TO phonon scattering is not allowed in the Raman spectrum. On the other hand, LO phonon scattering is forbidden from the (110) surfaces and TO phonon scattering is revealed.

3.3 RF power dependence on forbidden TO phonon

Figure 3.2 shows Raman spectra of the Ar ion beam etched InSb(100) surfaces at different RF powers. Each Raman spectrum was obtained from the etched InSb surface with various applied RF power from 50 to 200 W. The black line is the spectrum of the unetched InSb; red, blue, dark cyan and magenta lines are spectra of etched InSb wafers etched at 50, 100, 150 and 200 W RF power, respectively.

The peaks at 191 and 180 cm^{-1} are longitudinal optical (LO) and transverse optical (TO) phonon modes, respectively. The broad peak shown at 160 cm^{-1} originated from the amorphous InSb region. Raman measurements for the etched InSb surface show that the intensity of TO phonon modes was drastically enhanced as the RF power increases.

Scattering geometry	TO photon	LO photon
$x(y, y) \bar{x}; x(z, z) \bar{x}$	0	0
$x(y, z) \bar{x}; x(z, y) \bar{x}$	0	$ d_{LO} ^2$
$x(y', z') \bar{z}; x(z', y') \bar{x}$	0	0
$x(y', y') \bar{x}; x(z', z') \bar{x}$	0	$ d_{LO} ^2$

Table 3.3 Selection Rules for Zinc-blende materials on (100) surfaces.

According to the Raman selection rule for a zinc-blende crystal with (100) plane, the longitudinal optical (LO) phonon scattering is allowed and the TO phonon scattering should be forbidden. Thus, it represents that bombarding Ar ions break the Raman selection rule for InSb(100) and the degree of damages depend on the applied RF power in Ar-ion etching.

Fitting curves for the Raman spectra of the etched InSb with applied powers of 50 W and 200 W are represented in Fig.3.3 (a) and (b), respectively. The deconvoluted TO, LO and amorphous InSb (a-InSb) bands are represented by the Lorentzian curves. The TO scattering mode at 180 cm^{-1} which had to be forbidden for backscattering from a InSb(100) surface is observed and enhanced as increasing the RF power. Fig.3.3 (b) shows prominent TO mode peak compared to Fig.3.3 (a) and distinct a-InSb peak at the low-frequency side of the TO peak. The broad peak at 160 cm^{-1} originates from the highly damaged structure with destroyed long-range-ordering in the atomic arrangement.

To show the relation between Raman scattering and RF power more clearly, the ratio of the integrated area of the TO mode against and that of the LO mode ($I_{\text{TO}}/I_{\text{LO}}$) and the full width at half maximum (FWHM) of LO peak are plotted as a function of RF power in Fig.3.4.

The integrated area ratio of TO and LO peak (I_{TO}/I_{LO}) and the FWHM of LO peak were obtained from the fitting results. The left-side scale is for the integrated area ratio; the right-side scale is for the FWHM of the LO peak at 191 cm^{-1} .

Both the integrated area ratio of I_{TO}/I_{LO} and the FWHM of LO peaks are proportional to the applied RF power. In Fig.3.3 (b), the integrated area ratio of a-InSb peak and LO peak is about 0.22.

Figure 3.5 (a) and (b) shows the Raman spectra obtained from the same InSb wafer having different polarized direction of measuring. Fig. 1(a) was measured from the $x(y'z')\bar{x}$ polarized direction and (b) was obtained from the etched surface having $x(y'y')\bar{x}$ polarized direction, respectively. Each Raman spectrum represents the etched InSb(100) surface with different applied RF power of 50, 100, 150 and 200 W, respectively. Both spectra reveal the transverse optical (TO) phonon at 179.9 cm^{-1} and the longitudinal optical (LO) phonon at 190.8 cm^{-1} .

The parallel polarization geometry (a) shows the strong LO scattering and the very weak TO. On the other hand, the cross polarization geometry (b) shows the enhancement of TO scattering and

the distinct amorphous scattering more clearly. This is due to the Raman selection rule for (100) plane of zinc blende crystal.

In the Raman spectra of etched InSb(100) has a strong relation with plasma-induced defect and it was improved that polarized Raman spectra can show that difference more effectively.

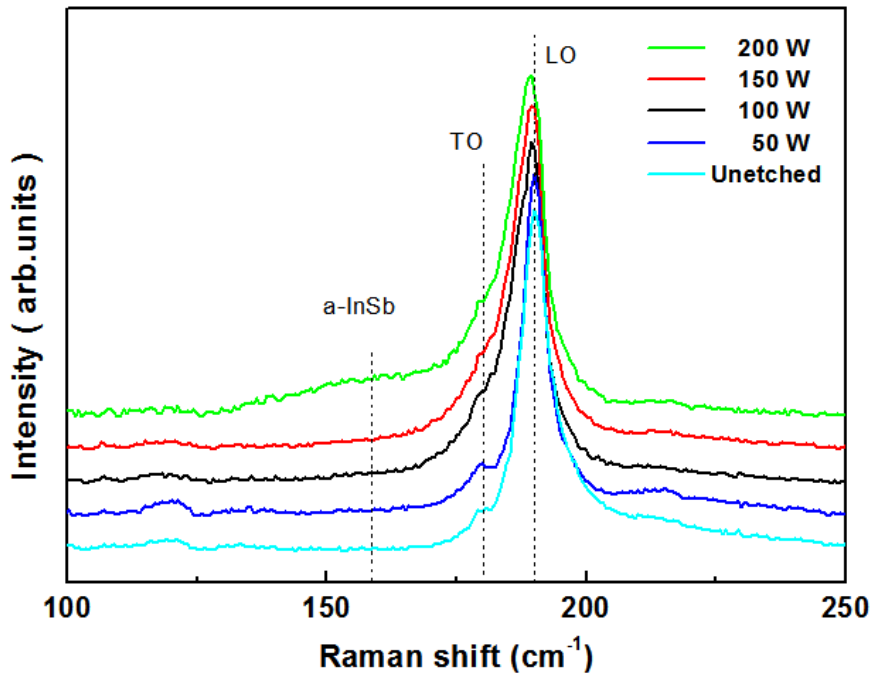


Fig.3.2 Raman spectra of Ar ion beam etched InSb surfaces with different RF power

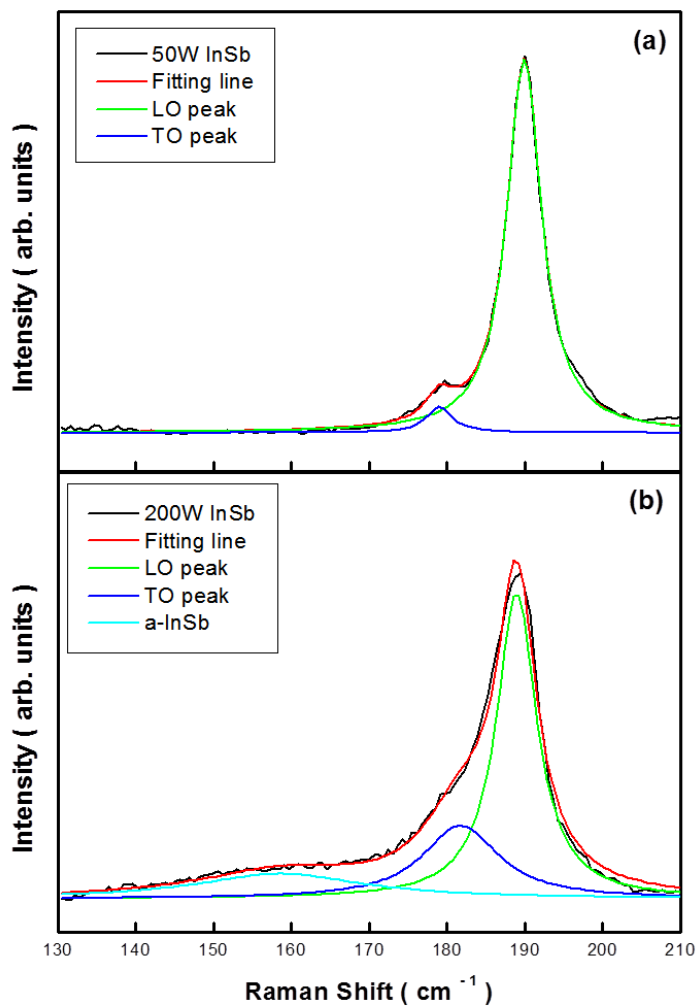


Fig.3.3 (a) Fitting curves for the Raman spectrum of the InSb etched at 50 W and (b) Fitting curves for the Raman spectrum of the InSb etched at 200 W. Each Lorentzian curve represents TO and LO peak, respectively.

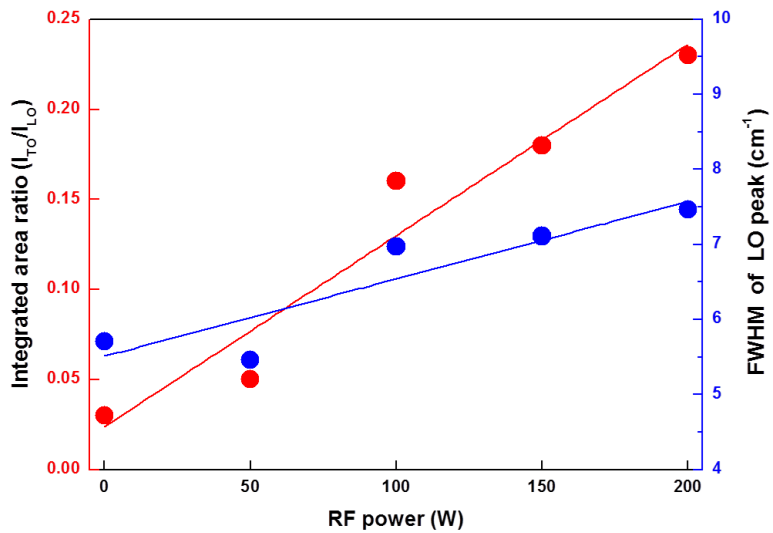


Fig.3.4. FWHM of LO peak (191 cm^{-1}) and integrated area ratio of TO peak and LO peak as a function of RF power.

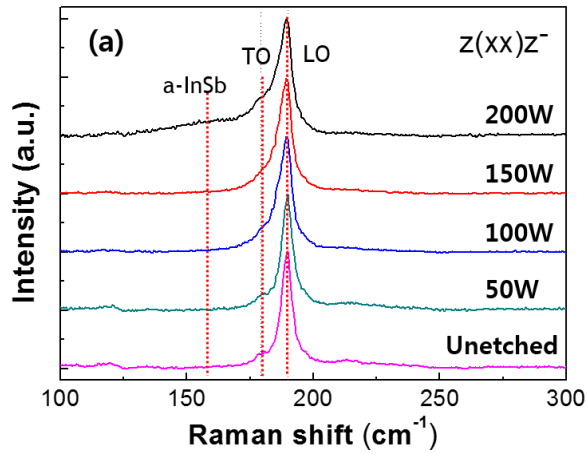
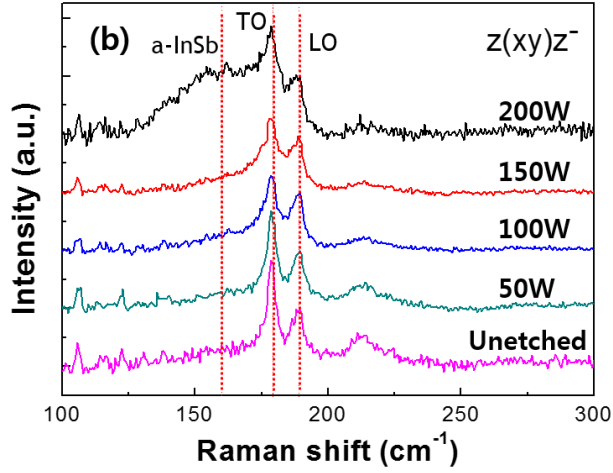


Fig.3.5 Polarized Raman spectra of Ar-ion beam etched InSb(100) surfaces (a) $x(y'z')\bar{x}$ direction and (b) $x(y'y')\bar{x}$ direction, respectively.

3.4 Origin of TO scattering enhancement

3.4.1 Existing hypothesis

This enhancement of TO phonon on etched surface was observed by F. Frost in 1999 [12]. However, it didn't explain the origin of this phenomenon clearly. According to their argument, the surface roughness is accompanied by the derivations from the backscattering geometry and results in the observations of the TO mode in Raman spectra.

Figure 3.6 illustrates the relation between enhancement of TO phonon and surface roughness. The breaking of the Raman selection rule is caused by the partly disordered structure and the roughened surface leading to local enhancement of the forbidden TO phonon scattering in Raman spectrum. Especially, as the etched surface being rougher, due to the existence of nano-sized facets, the refraction effects can be occurred. It induces the change of propagation direction of light in the crystal. As a result, unexpected TO phonon scattering can be observed in Raman spectrum of InSb (100) plane. Table 3.4 shows the Refractive index of InSb with 514 nm wavelength.

However, as shown in the Fig. 3.7 and Fig. 3.8, it was proven

that there is no tight relation between surface roughness and TO phonon scattering enhancement in the Raman spectrum. Figure 3.6 shows the morphology of etched InSb(100) surfaces measured by atomic force microscopy (AFM) and Figure 3.8 represents the relationship between surface roughness and TO scattering enhancement as a function of RF power. The value of root-mean-square (RMS) roughness of the etched InSb surface decreased from 4.43 nm to 1.02 nm and, however, the integrated area ratio of normalized TO and LO peak increased from 0.05 to 0.23 with increasing RF power from 50 W to 200 W. It definitely means that the enhancement of TO modes originated from other factor not surface morphology.

3.4.2 Defect related with preferential loss of Sb

To examine the origin of enhanced TO phonon scattering in the Raman spectrum, etched InSb wafer was annealed at antimony (Sb) ambient for 30 min using metal-organic chemical vapor deposition (MOCVD). Figure 3.9 indicates the Raman spectrum of etched InSb(100) wafer before and after annealing process. The black spectrum was taken from an as-etched sample. The red spectrum was taken from the etched

sample after annealing at 450°C. The blue spectrum was taken bare sample and inserted as a reference.

Thus, it is reasonable to think that the break-down of the selection rule is caused by the structurally damaged area. The structural disordering due to induced-defects breaks the symmetry of the crystal and would lead to break the rule.

As discussed by *Sendra et al.*[14], Sb vacancies caused by preferential sputtering can account for the increase of the number of defects near the etched surface. The structural disordering due to induced-defects breaks the symmetry of the crystal and would lead to break the rule. After annealing under antimony ambient, the intensity of enhanced TO mode was fully restored back and it became close to that of the unetched state. These results demonstrate that it is the Sb vacancy among the defects caused by the plasma etching that caused the forbidden TO phonon scattering to reveal in the Raman spectrum of InSb(100) surface.

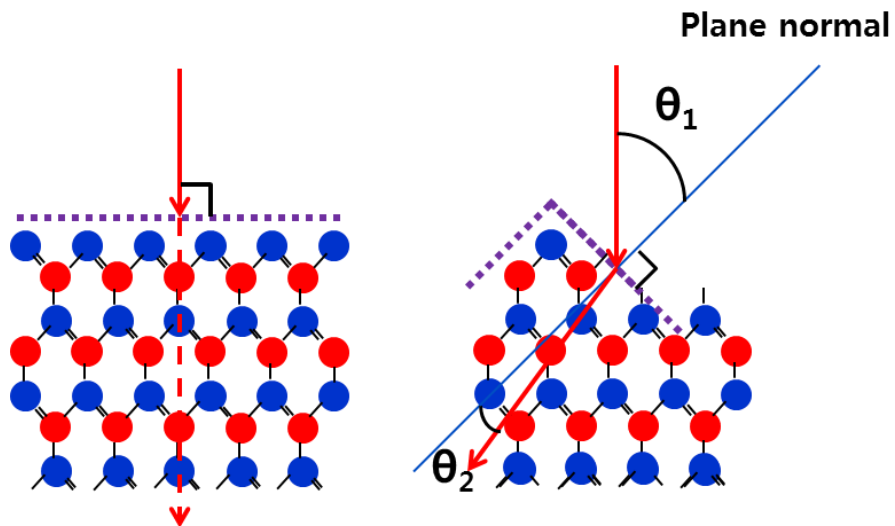


Fig.3.6 Propagation of incident light at flat surface and rough surface.

Wave length (nm)	n	k
511.73	3.743	2.282
514.5	3.7902	2.280
520.46	3.892	2.276

Table 3.4 Refractive index of 514 nm laser of InSb.

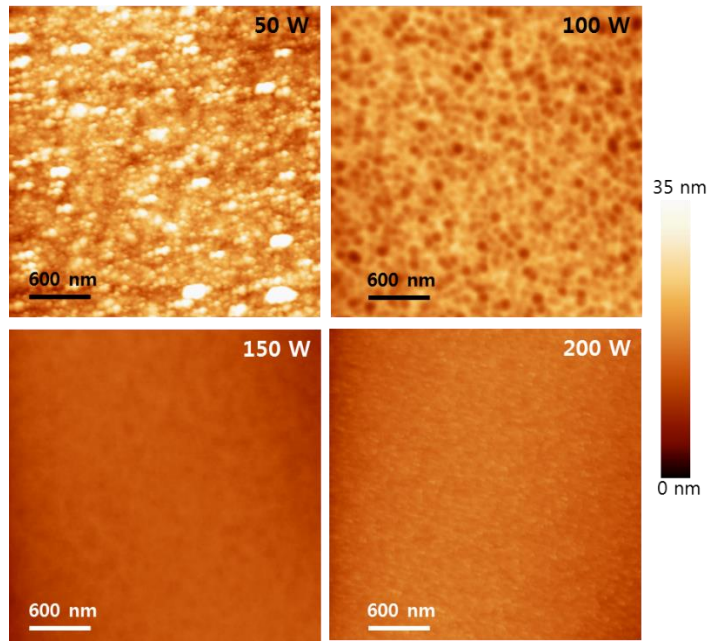


Fig. 3.7 Atomic Force Microscope (AFM) images of Ar ion beam etched InSb surfaces with different RF power.

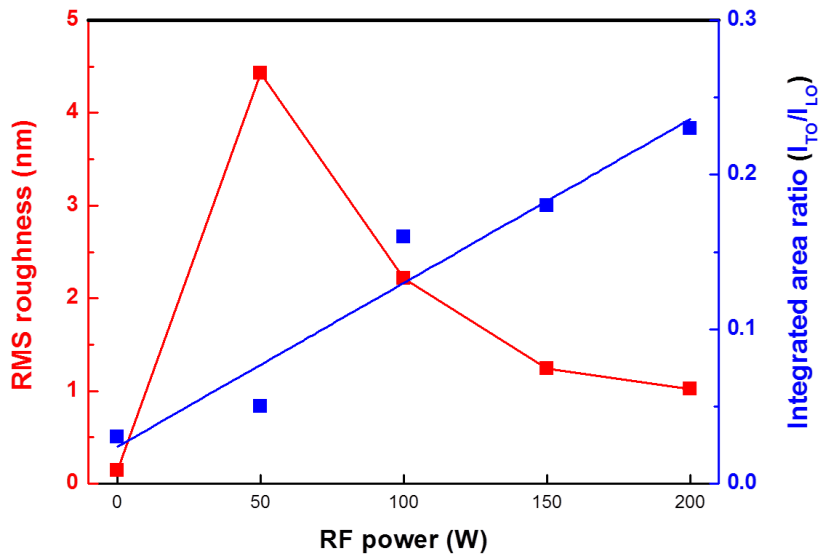


Fig. 3.8 Relationship between surface roughness and TO phonon enhancement.

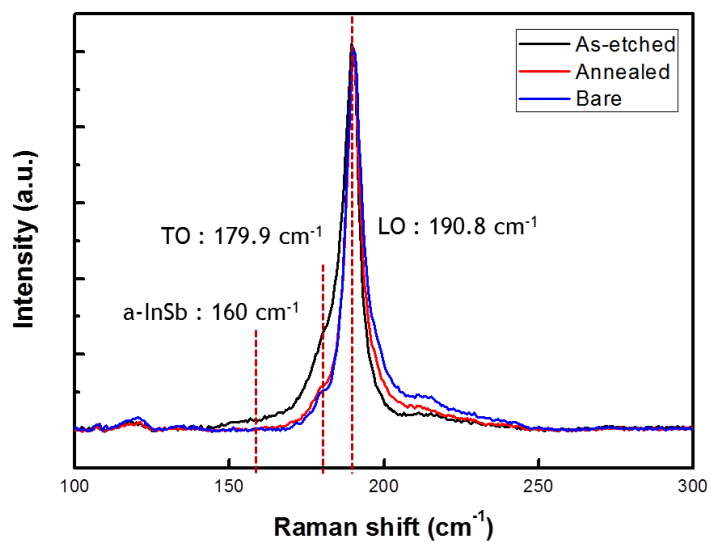


Fig. 3.9. Raman spectra of the as-etched InSb(100) and damage-annealed InSb(100).

3.5 Summary

In this chapter, plasma-induced defect on InSb surface was studied. To measure the fine defect existing beneath the surface within a few nanometer thickness, Raman spectroscopy was adopted. Because the information about the small amount of surface defect could be obtained clearly due to the relatively short penetration depth of the incident laser beam of 514.5 nm wavelength, in crystalline InSb. Thus, by applying this analysis method to our research, even a small amount of surface defect generated by plasma during plasma etching process could be analyzed effectively.

As a result, by measuring the degree of enhancement of TO scattering, theoretically it has to be forbidden in the spectra of (100) plane, the information related with plasma-induced defect were obtained effectively. Moreover it was also shown that the number of defect was tightly depending on the energy of plasma. Furthermore, it was demonstrated that the origin of enhanced TO phonon scattering is plasma-induced defects such as Sb vacancy due to the preferential loss of Sb atoms.

In conclusion, it is experimentally proven that Raman spectroscopy is effective method for evaluating the plasma-induced defects originated from the loss of Sb atom for the first time.

3.6 References

- [1] H. J. Bowley, D. J. Gardiner, D. L. Gerrard, P. R. Graves, J. D. Loudon, and G. Turrell, *Practical Raman Spectroscopy*, Springer-Verlag, (1986).
- [2] K. M. Chang, J. J. Luo, C. D. Chiang, and K. C. Liu, *J. J. Appl. Phys.* **Vol. 45**, No. 3, 1477 (2006).
- [3] G. D. Zhang, W. G. Sun, S. L. Xu, H. Y. Zhao, H. Y. Su, and H. Z. Wang, *J. Vac. Sci, Technol. A* **27**, 681 (2009).
- [4] G. B. Stringfellow, *J. Vac. Sci. Technol.* **Vol. 13**, No. 4, 908 (1976).
- [5] L. P. Chen, J. J. Luo, T. H. Liu, S. P. Yang, Y. M. Pang, and S. J. Yang, *Jpn. J. Appl.* **Vol. 31**, 813 (1992).
- [6] S. J. Fonash, *J. Electrochem. Soc.* **Vol. 137**, No. 12, 3885 (1990).
- [7] J. R. Mileham, J. W. Lee, E. S. Lambers, and S. J. Pearton, *Semicond. Sci. Technol.* **12**, 338 (1997).
- [8] F. Frost, A. Schindler, and F. Bigl, *Semicond. Sci. Technol.* **13**, 523 (1998).
- [9] B. Kim, and B. Lee, *IEEE Transactions on Plasma Science* Vol. 30, No. 5, 2074 (2002).
- [10] A. S. Yapsir, G. F. Wiltshire, J. P. Gambino, R. H. Kastl, and C.

- C. Parks, *J. Vac. Sci. Technol. A* **8**, 2939 (1990).
- [11]J. L. Birman, *Phys. Rev.* **Vol. 131**, No 4, 1489 (1963).
- [12]F. Frost, G. Lippold, A. Schindler, and F. Bigl, *J. Appl. Phys.* **Vol. 85**, No 12, 8379 (1999).
- [13]J. S. Lannin, *Solid State Communications* **Vol. 11**, 1523 (1972).
- [14]A. Kailer, K. G. Nickel, Y. G. Gogotsi, *J. Raman Spectrosc.* **30**, 939 (1999).
- [15]I. Zardo, S. C. Boj, F. Peiro, J. R. Morante, J. Arbiol, E. Uccelli, G. Abstreiter, and A. F. Morral, *Phys. Rev. B* **80**, 245324 (2009).
- [16]C. J. Kiely, J. I. Chyi, A. Rockett, and H. Morkoc, *Philosophical Magazine A* **Vol. 60**, No. 3, 321 (1989).
- [17]Z. C. Feng , S. Perkowitz, T. S. Rao, J. B. Webb, *J. Appl. Phys.* **68**, 5363 (1990).
- [18]E. Liarokapis, and E. Anastassakis, *Phys. Rev. B* **Vol. 30**, No. 4, 2270 (1984).
- [19]J. R. Sendra, G. Armelles, T. Utzmeier, J. Anguita, and F. Briones, *J. Appl. Phys.* **79**, 8853 (1996).
- [20]A. Pinczuk, and E. Burstein, *Phys. Rev. Lett.* **Vol. 21**, No. 15, 1073 (1968).
- [21]R. C. C. Leite, and J. F. Scott, *Phys. Rev. Lett.* **Vol. 22**, No. 4, 130 (1969).
- [22]T. Nakagawa, K. Ohta, N. Koshizuka, *Jpn. J. Appl. Phys.* **19**, L339 (1980).
- [23]V. K. dixit, B. V. Rodrigues, H. L. Bhat, R. Kumar, R. Venkataraghavan, K.S. Chandrasekaran, and B. M. Arora, *J. Appl. Phys.* **Vol. 90**, No 4, 1750 (2001).
- [24]G. P. Schwartz, *Thin Solid Films* **103**, 3 (1983).

Chapter 4.

Antimony (Sb) segregation

4.1 Motivation for thermal reaction study

In order to fabricate InSb devices, a number of deposition process and annealing process are required such as metal deposition, passivation and activation. However, due to the very low melting temperature of 525°C and weak binding energy between indium (In) and antimony (Sb) atoms, it can be easily deformed and damaged by irradiated thermal energy during the fabrication process. Especially, the structural deformation causes the change of material properties and the degradation of device performance.[1]

The efforts towards damage reduction induced by external heat are having great importance as the application of InSb expands to large area newly demanded. Unfortunately, the mechanism of structural modification induced by thermal energy during the fabrication process has not reported clearly yet. In this paper, during the annealing process, the *in-situ* monitoring of InSb surface by using Raman spectroscopy was investigated.

4.2 In-situ analysis of Sb segregation

4.2.1 In-situ monitoring of Sb segregation

In order to clarify the mechanism for phase change during annealing, effects of irradiated thermal energy on InSb surface were investigated in this study. According to *M. Hunermann et al.*[14], Sb monolayer can be detected by Raman spectroscopy effectively. Thus, to observe visually the process of the formation of elemental Sb and the segregation of it, a micro-Raman technique was used. With raising the temperature from 25 to 500°C, phase change of InSb near the surface during annealing process were examined by in-situ Raman spectroscopy. Furthermore collecting spectral data with spatial resolution and encoding it in a 2D plot generates images with information complementary to optical imaging. By using this we can observe the segregation step

Figure 4.1 represents the *in-situ* Raman spectra of InSb(100) surface with raising the temperature. Each Raman spectrum was obtained from the InSb surface of same sample with raising temperature from room temperature to 500°C. Each colored line is the spectrum measured at 25, 100, 200, 300, 400, 450, and 500°C, respectively. The two peaks

at 180 and 191 cm^{-1} correspond to the TO and LO modes of InSb, respectively. [2] With increasing the temperature, the position of LO and TO peak were shifted to the lower wavenumber side of normal position the full width at half maximum (FWHM) were increased due to the temperature dependence.[3,4] The degree of shift is strongly depending on the environmental temperature. After reaching the temperature of 450°C, it showed a broad peak around 145 cm^{-1} similar to the Raman spectrum of the amorphous antimony (Sb) peak.[5] Furthermore, as the temperature increasing from 450 to 500°C, the amorphous peak was split up into distinct two peaks. These two peaks are typical peaks of crystalline Sb having the LO (150 cm^{-1}) and TO (115 cm^{-1}) phonon modes.[6]

In Figure 4.2, the comparative spectra and images of InSb surfaces before and after annealing process were shown more clearly. There was an obvious contrast between the Raman spectra of before and after annealing as shown in Fig. 2(a). The prominent TO and LO mode of elemental Sb were still remained when it cooled down. It is a strong evidence of Sb segregation originated from the chemical reaction at high temperature. Moreover, the 1 x 1 μm^2 of AFM image of InSb surface without annealing is represented in Fig. 2(b) and that of InSb surface

which was cooled back down to room temperature after reaching the highest temperature of 500°C was shown in Fig. 2(c). The value of root-mean-square (RMS) roughness of measured surface was dramatically changed from 0.1054 nm to 3.6709 nm after reaching the 500°C and then cooling down to the room temperature.

It was reported by *M. Tomisu et al.*[7] that the surface of InSb was roughened by annealing due to the re-evaporation of Sb atoms. Generally, the preferential loss of Sb near the surface was well known phenomenon due to the higher vapor pressure of group V material and it resulted in rough surface.[8,9] However, in this case, it could not explain the distinct Raman peaks of Sb which still remained with the dominant Raman peak of InSb.

Figure 4.3 indicates the 2-D mapping results of Sb peak. An optical image of InSb surfaces measured at different temperature, with the corresponding Raman image, is also shown in this figure. Raman mapping of Sb peak represented that the number of elemental Sb was increased drastically as the temperature increasing from 450 to 500°C, respectively. It showed clearly that the grain of elemental Sb was grown gradually with temperature raising, and when the temperature exceed 500°C, the whole surface of InSb was covered elemental Sb.

As clearly shown in this figure, Sb segregation began to occur and grew up gradually as the temperature increasing from 450 to 500°C. Finally the whole surface was covered with segregated Sb phase.

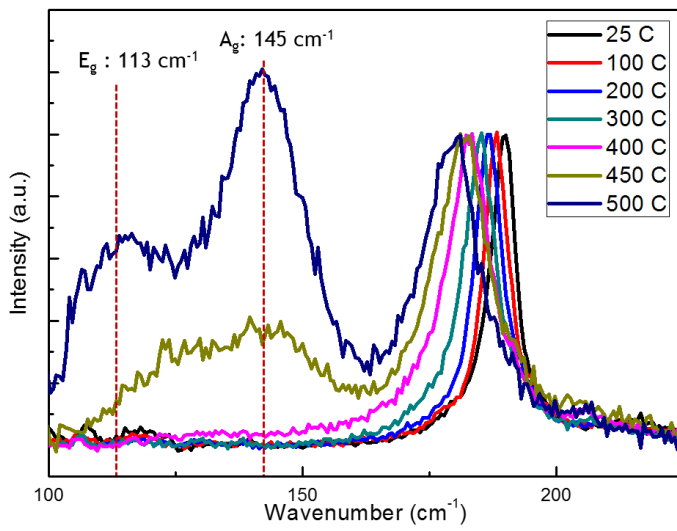


Fig. 4.1. *In-situ* Raman spectra of InSb(100) surfaces with increasing temperature.

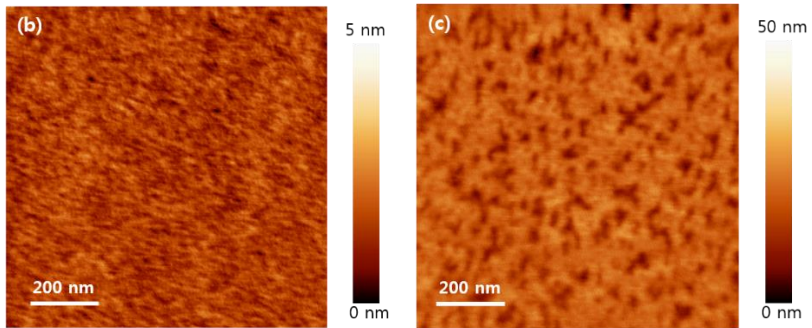
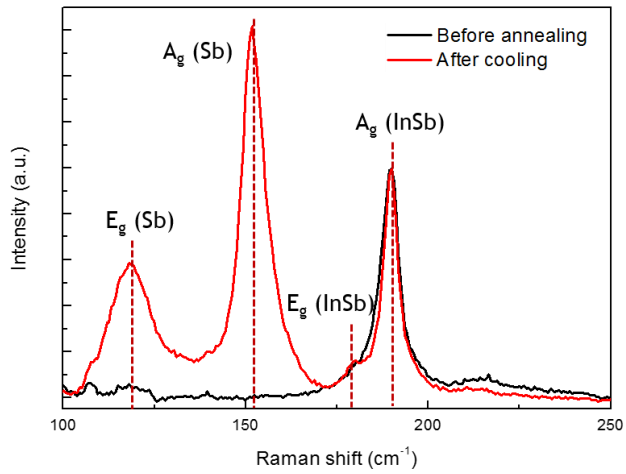


Fig. 4.2. Comparison of surface properties before and after annealing process. (a) comparison of Raman spectra and (b, c) comparison of AFM images.

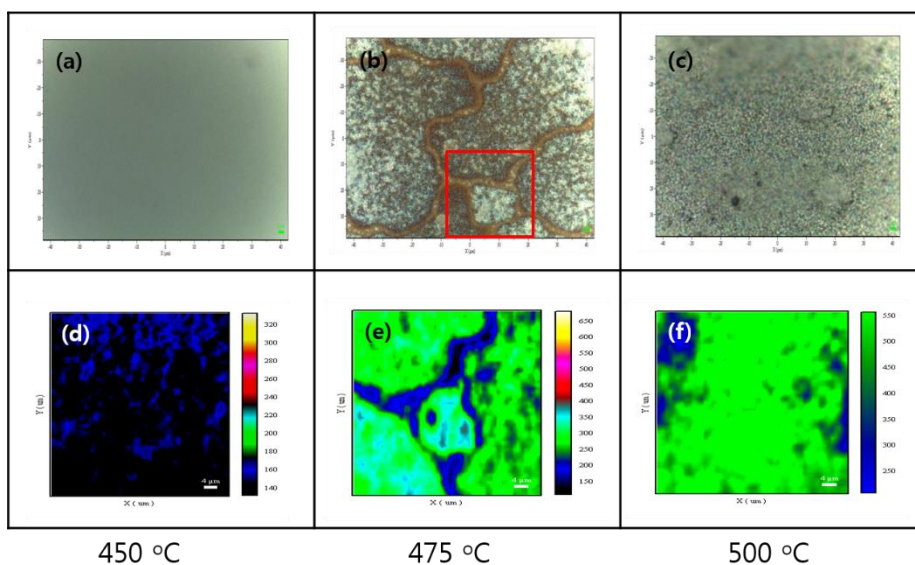
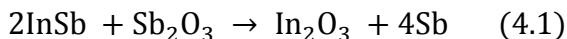


Fig. 4.3. Optical microscopy images and 2-D Raman map images of InSb surfaces measured at 450, 475 and 500°C. Optical microscope images of annealed InSb surface observed at (a) 450, (b) 475 and (c) 500°C. 2-D Raman map of the spectrum integrated between 140 and 160 cm^{-1} , which can be assigned to the E_g phonon in elemental antimony(Sb) obtained at (d) 450, (e) 475 and (f) 500°C.

4.2.2 Chemical reaction on the surface

In order to find the origin of elemental Sb peak in the Raman spectra, the chemical composition of InSb was analyzed by using AES depth-profiles. Figure 4.4 shows the composition profile of InSb surface before and after *in-situ* annealing at 500°C analyzed by Auger Electron Spectroscopy (AES). As Sb has a higher sputtering rate and vapor pressure, it escaped out prior to In so that the atomic composition of Sb and In in AES profiles of InSb crystal showed a slight difference in stoichiometry even in the bare samples.[13] Fig. 3(a) indicates the composition of InSb surface measured at 25°C before annealing and Fig. 3(b) shows that of cooled sample measured at the same temperature after annealing. Since the thermal decomposition at high temperature and following chemical reaction with native oxides:



is favored, as a result, an excess of elemental Sb was segregated between InSb substrate and native oxide layer in AES profiles of annealed sample[10-12]. Thus, the two phonon modes of elemental Sb phase

shown in Fig. 4.1 and 4.2(a) were originated from the segregated Sb due to the thermal decomposition of InSb substrate and the following chemical reaction with native oxides including In_2O_3 .

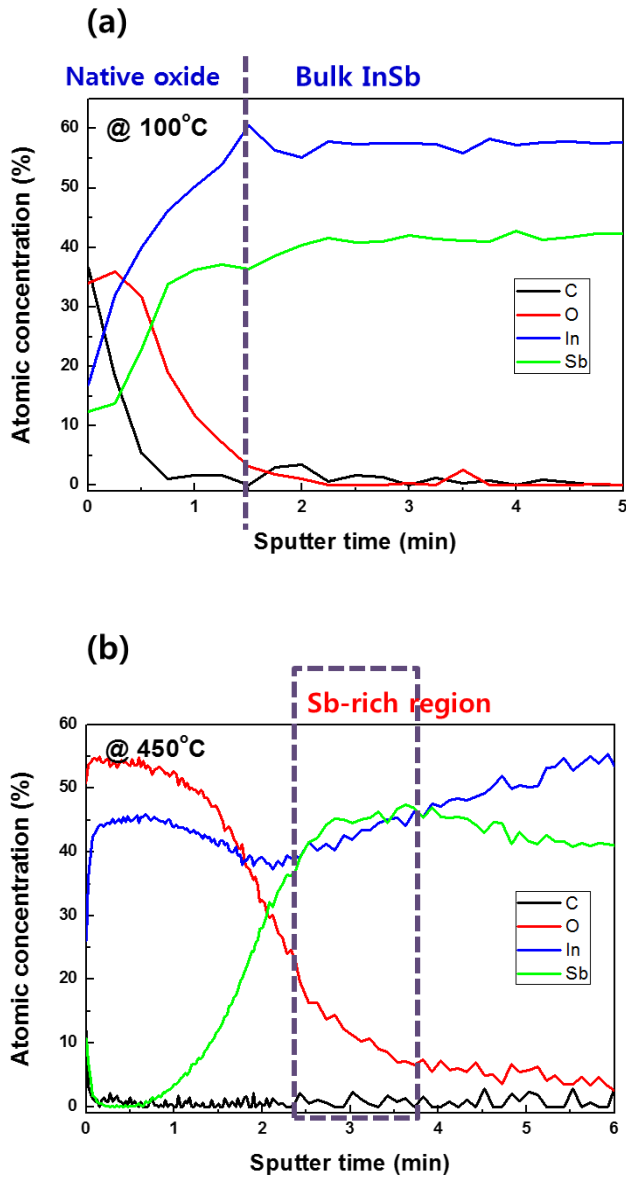


Fig. 4.4. Composition profile of InSb surface (a) before and (b) after annealing process analyzed by AES. Ar-ion sputtering rate is about 1 – 1.5 nm/min.

4.3 Temperature and Time dependence on Sb segregation

Figure 4.5 represents the ex-situ Raman spectrum of RTA annealed InSb for 2.5 minutes with increasing the annealing temperature from 100 to 500°C. Above 400°C, two peaks of elemental Sb began to observe in the spectrum. Especially, when the temperature was higher than 450°C, main peak of InSb substrate disappeared. The penetration depth in crystalline InSb is about 8.9 nm, thus it can be predicted indirectly that the thickness of Sb phase increased with temperature raising.

Figure 4.6 represents the ex-situ Raman spectrum of RTA annealed InSb at 300 °C with increasing the annealing time from 5 to 25 minutes. As the time increasing gradually, the Sb phase began to observe. Even at the low temperature of 200 °C, in the long-time annealed surface for 2 hours, a small amount of segregated Sb was detected.

Both temperature and time can be critical factors affecting the reaction, thus it means that the temperature should be kept at below 250 °C to avoid the segregation during annealing process.

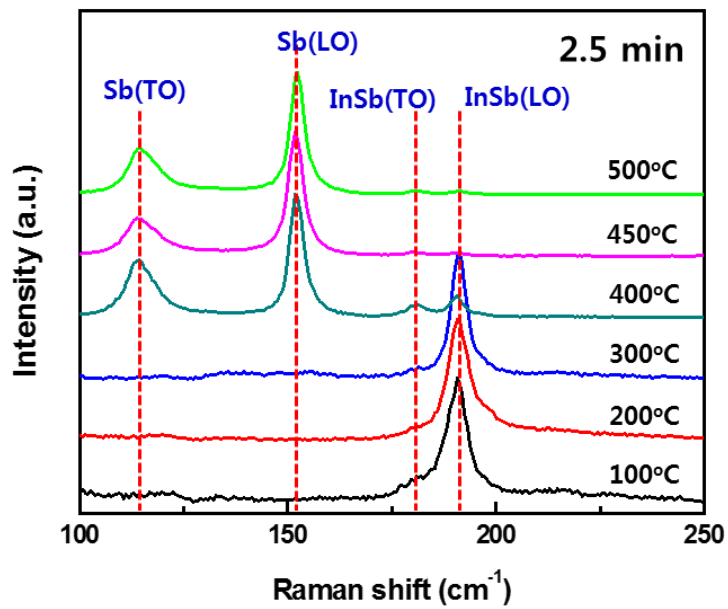


Fig. 4.5. Raman spectra of RTA-annealed InSb(100) surfaces for 2.5 minutes with increasing temperature.

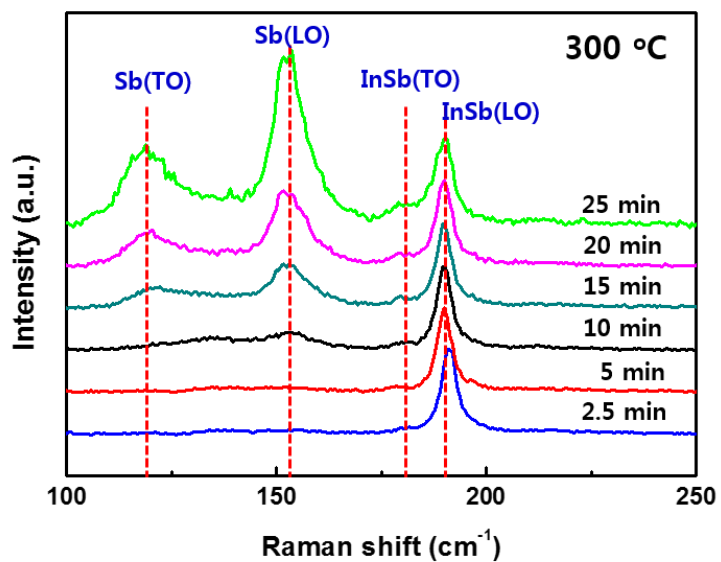


Fig. 4.6. Raman spectra of RTA-annealed InSb(100) surfaces at 300°C with increasing time.

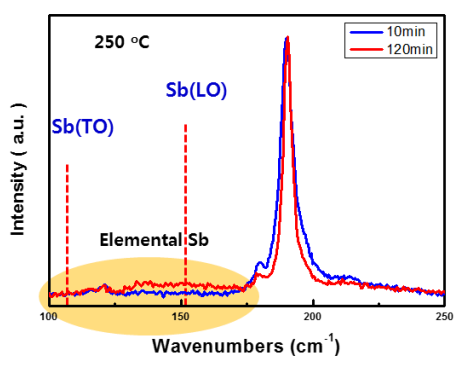
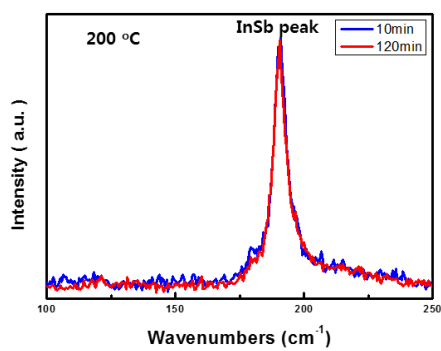
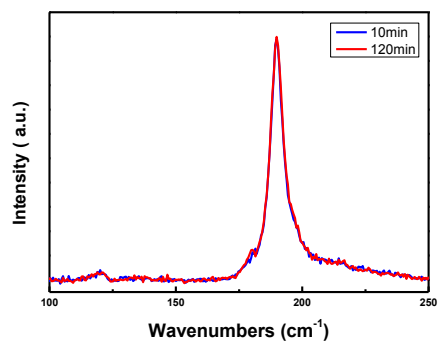


Fig. 4.7. Raman spectra of long time-annealed InSb(100) surfaces.

4.4 Summary

In this chapter, thermally generated defect on InSb surface was studied. To find the origin of thermal defect and the solution preventing the generation, InSb surface was investigated with the temperature increasing. By the *in-situ* monitoring using Raman spectroscopy and 2-D peak mapping of InSb surface during annealing process, antimony segregation was clearly examined and it was demonstrated that the Sb phase formed on the surface due to the thermally generated chemical reaction of InSb with Sb_2O_3 . Above the temperature of 450°C , Sb phase was observed in the Raman spectra. Especially, 2-D mapping of Sb peak represented the continuous steps of the formation of Sb phase visually.

The chemical composition was analyzed by AES depth-profiles and it was indicated that Sb phase was existed between native oxides and InSb substrate. It was predicted that the thickness of Sb layer is about 3-5 nm. The segregation of Sb had a strong relation with temperature and time.

In conclusion, due to the chemical reaction with native oxide during annealing process, it was proved that segregated Sb phase was formed on the surface at high temperature above 400°C or at relative

lower temperature with long-annealing time. Thus, it means that, to avoid the segregation, the annealing temperature have to be kept below 250°C during fabrication process.

4.5 References

- [1] C. Seok, S. Kim, J. Lee, S. Park, Y. Park, and E. Yoon, *MRS Proceedings*, **1670** (2014).
- [2] C. Seok, M. Choi, S. Park J. Jung, Y. Park, I. Yang, E. Yoon, *ECS Solid State Letters*, **3**, No. 3, 27-29 (2014).
- [3] W. S. Li, Z. X. Shen, Z. C. Feng, and S. J. Chua, *J. Appl. Phys.*, **87**, No. 7, 3332-3337 (2000).
- [4] J. Menendez, and M. Cardona, *Phys. Rev. B*, **29**, No. 4, 2051-2059 (1984).
- [5] C. Gatzke, S. J. Webb, K. Fobelets, and R. A. Stradling, *Semicond. Sci. Technol.* **13**, 399-403 (1998).
- [6] U. Rossow, U. Frotscher, N. Esser, U. Resch, T. Muller, and W. Richter, *Appl. Surf. Sci.* **63**, 35-39 (1993).
- [7] M. Tomisu, N. Inoue, and Y. Yasuoka, *Vacuum* **47**, No. 3, 239-242 (1996).
- [8] S. Park, J. Jung, C. Seok, K. W. Shin, S. H. Park, Y. Nanishi, Y. Park, and E. Yoon, *J. Crystal Growth*, (2013).

- [9] R. M. Biefeld, *Mater. Sci. Eng. R* **36**, 105-142 (2002).
- [10] T. P. Smirnova, A. N. Golubenko, N. F. Zacharchuk, V. I. Belyi, G. A. Kokovin, and N. A. Valisheva, *Thin Solid Films*, **76**, 11-21 (1981).
- [11] R. P. Vasquez, and F. J. Grunthaner, *J. Vac. Sci. Technol.*, **19**, 431-436 (1981).
- [12] E. Valcheva, *J. Vac. Sci. Technol. A* **15**, 5, 2489-2491 (1997).
- [13] J. Liu, and T. Zhang, *Appl. Surf. Sci.* **126**, 231-234 (1998).
- [14] M. Hunermann, J. Geurts, and W. Richter, *Phys. Rev. Lett.* **66**, 5, 640-643 (1991).

Chapter 5.

Reduction of process-induced defect

5.1 Plasma etching

5.1.1 Comparison of conventional etching methods

To verify the effectiveness of conventional methods and to find the most suitable method for InSb, a comparative research on various plasma etching for InSb was examined. To evaluate the suitability of conventional etching methods for InSb, reactive ion beam etching (RIE) and ion beam etching (IBE) with CH₄/H₂/Ar gas mixture, Cl₂/Ar gas mixture, Ar gas and N₂ gas were investigated.

Figure 5.1 shows the etched surface morphology characterized by AFM. It showed the values of root-mean-square (RMS) roughness obtained from samples etched by different methods above were 18.6596 nm, 8.9654 nm, 1.9935 nm and 0.4121 nm, respectively. In the case of RIE with CH₄/H₂/Ar and Cl₂/Ar gas mixture, by-products such as carbide and chloride were formed on the etched surface and these compounds made the surface rough [2-4]. And these artifacts can act as defects or

trap sites causing the degradation of InSb devices. On the other hand, relatively smooth surfaces having less artifacts were obtained after the etching process with Ar and N₂ plasma. In the sense of surface morphology after etching process, it seemed that Ar IBE and N₂ RIE was relatively more effective method for InSb among conventional methods.

However, when it compared to the values reported by Frort et al. [6], the measured values were relatively larger than that. Due to this reason, in order to find the more optimized condition for InSb, the intensive experiments on Ar IBE and N₂ RIE were conducted with changing the RF power from 50 to 200 W. Figure 5.2 represent the AFM images of the etched surface at different RF powers of 50, 100, 150 and 200 W, respectively. Fig. 5.2 (a), (b), (c) and (d) were obtained from the samples etched using Ar IBE and Fig. 5.2 (e), (f), (g) and (h) were obtained from those etched using N₂ RIE. The values of RMS roughness were shown in the figures.

To illustrate clearly the effect of RF power on etching properties, these measured etch rate and RMS roughness were plotted. Figure 5.3 shows the change of etch rate and RMS roughness values as a function of RF power. When it compared to Ar IBE, it was clear that N₂ RIE process resulted in the smoother and less damaged surface, however, the

etch rate of the N₂ RIE (10-15 nm/min) was much lower than that of Ar IBE (70-80 nm/min) as shown in Fig. 5.3. Despite the better etching results, considering 1 μm-thick mesa-etching requirement, this slow etching rate would be a barrier to tackle. In the case of Ar IBE, on the other hand, plasma-induced defect would be an obstacle for the highly sensitive InSb detectors to solve. Especially, when the RF power was above 200 W, it was proven that amorphous InSb phase were formed on the surface by irradiated Ar ions [7].

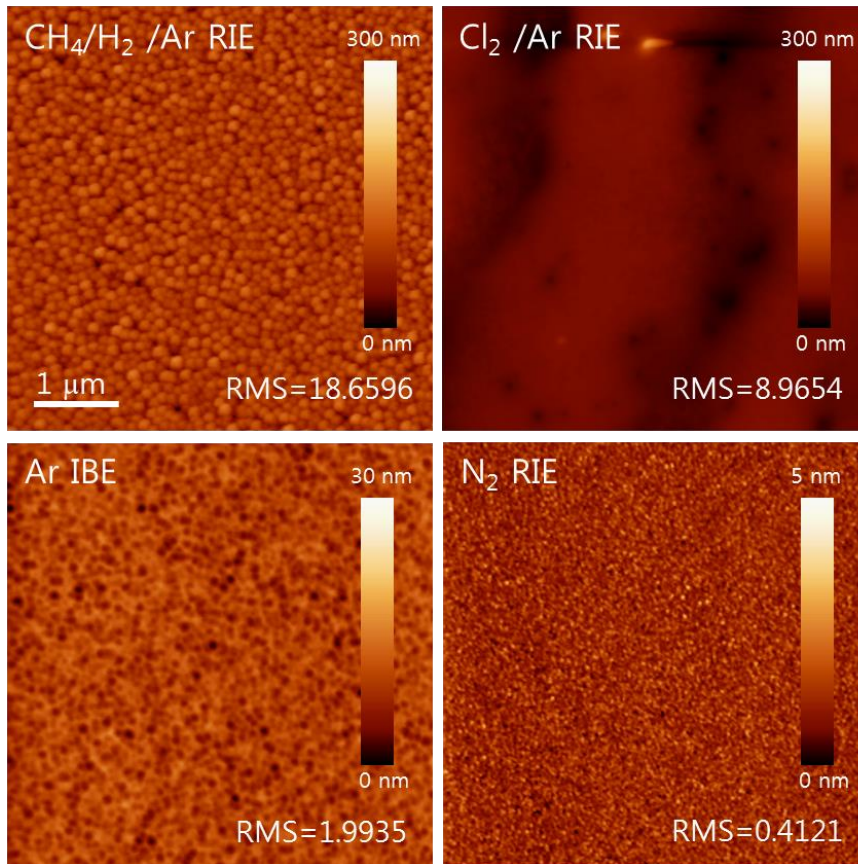


Fig. 5.1. AFM images of plasma-etched InSb surfaces using (a) CH₄/H₂/Ar RIE, (b) Cl₂/Ar RIE, (c) Ar IBE, and (d) N₂ RIE.

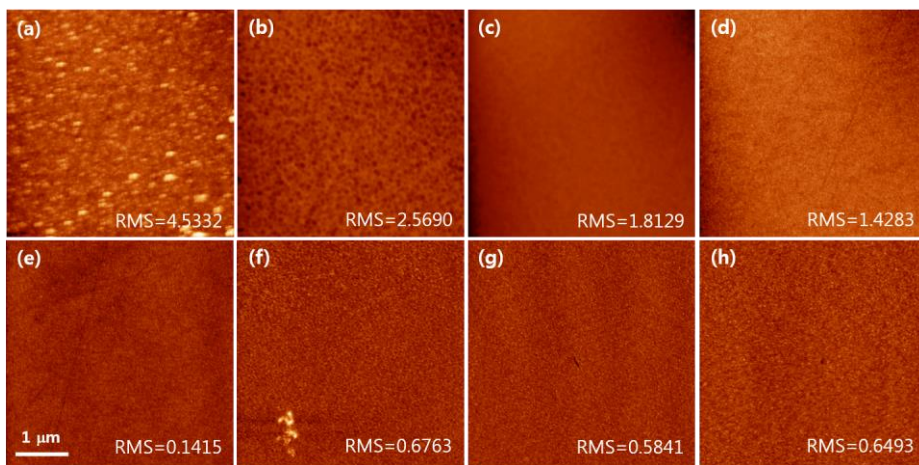


Fig. 5.2. AFM images of plasma-etched InSb surfaces using Ar IBE and N₂ RIE as increasing RF power. (a), (b), (c) and (d) show the etched surface using Ar IBE at 50, 100, 150 and 200 W, respectively. The etched surface using N₂ RIBE at 50, 100, 150 and 200 W are shown in (e), (f), (g) and (h), respectively.

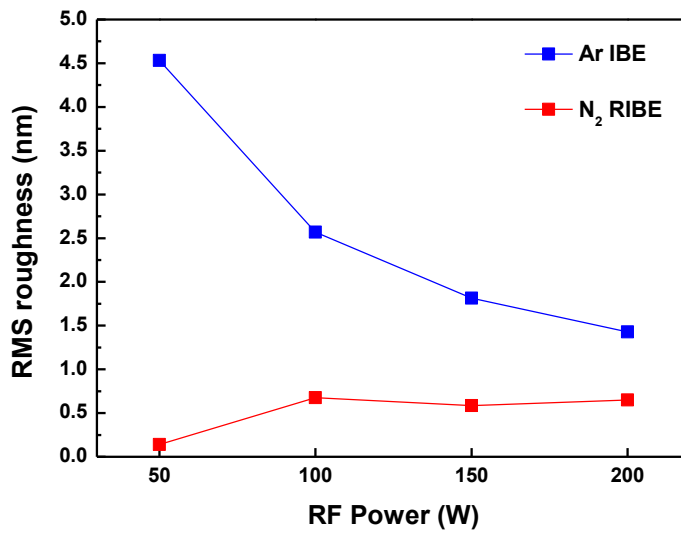
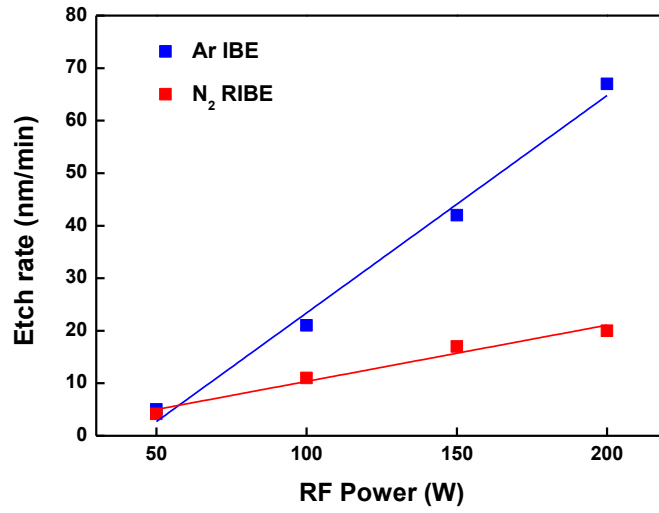


Fig. 5.3. Etch rate and surface roughness as a function of RF power.

5.1.2 Multi-step plasma etching (MSE) process

To overcome these limit of conventional techniques and satisfy both requirements of fast etch rate and smooth surface with lower plasma-induced defects, a multi-step etching (MSE) process, a combination of the Ar etching and the N₂ etching, is developed as a solution.

Figure 5.4 shows the concept of this new method. In order to combine the advantages of the two methods, the MSE process was sequentially performed at Ar, Ar : N₂ =1 : 1, Ar : N₂ =1 : 2, and N₂ ambient for 15, 5 ,3, 1 minutes, respectively. Due to the first step using Ar IBE, the fast etch rate can be retained. When the amount of N₂ gas flow was gradually increased during the etching process, the RMS roughness decreased dramatically.

Figure 5.5 shows the change of surface roughness during MSE process. In the Fig. 5.5, the image of (a), (b), (c) and (d) obtained from as-etched InSb surface after 1st, 2nd, 3rd, and 4th step in the MSE process, respectively. Figure 5.6 represents the change of etch rate and RMS roughness during MSE process more clearly.

As a result, the MSE process can generate relatively flat surface with lower RMS roughness (about 0.209 nm) than the surface etched by Ar IBE (1.8129 nm). Furthermore, figure 5.7 indicates the comparison results of Raman spectrum between Ar IBE and MSE. As shown in the figure, MSE method reduced the plasma-induced defects compared to conventional Ar IBE method. The calculated values obtained from Raman spectra in Fig. 5.7 such as integrated area ratio of A_{TO}/A_{LO} , FWHM and peak position of LO peak. The integrated area ratio decreased from 0.15 to 0.06. In the previous chapter, the origin of enhanced TO phonon is plasma-induced defects induced by preferential loss of Sb atoms. Thus, the reduction of A_{TO}/A_{LO} means that the defects induced by plasma during etching process decreased when MSE was used instead of conventional Ar IBE method.

These results imply that the MSE process is more effective in reducing the surface damage induced by ion-etching than the conventional methods.

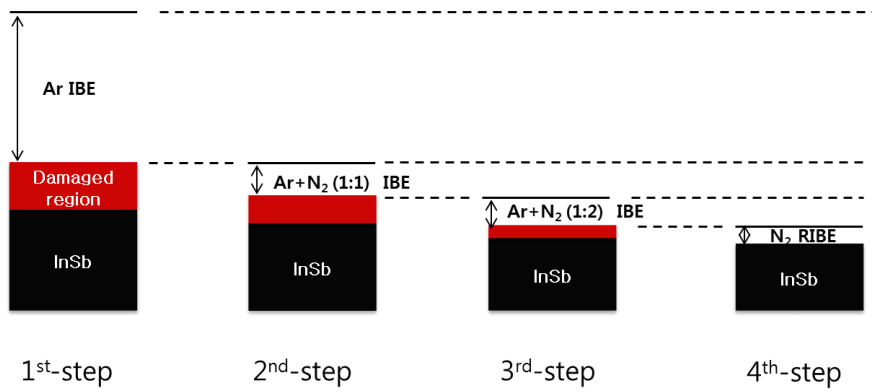


Fig. 5.4. Process flow of multi-step etching process.

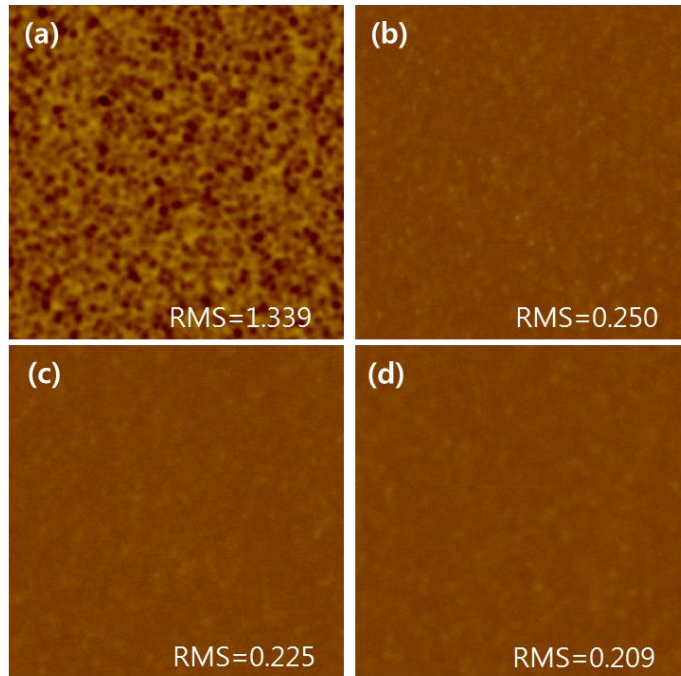


Fig. 5.5. Surface morphology change during MSE process.

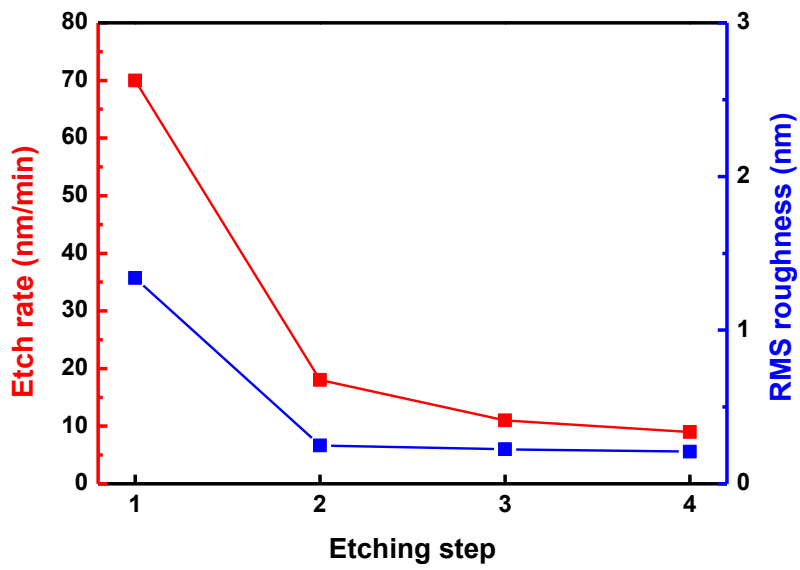


Fig. 5.6. Etch rate and RMS roughness change during MSE process.

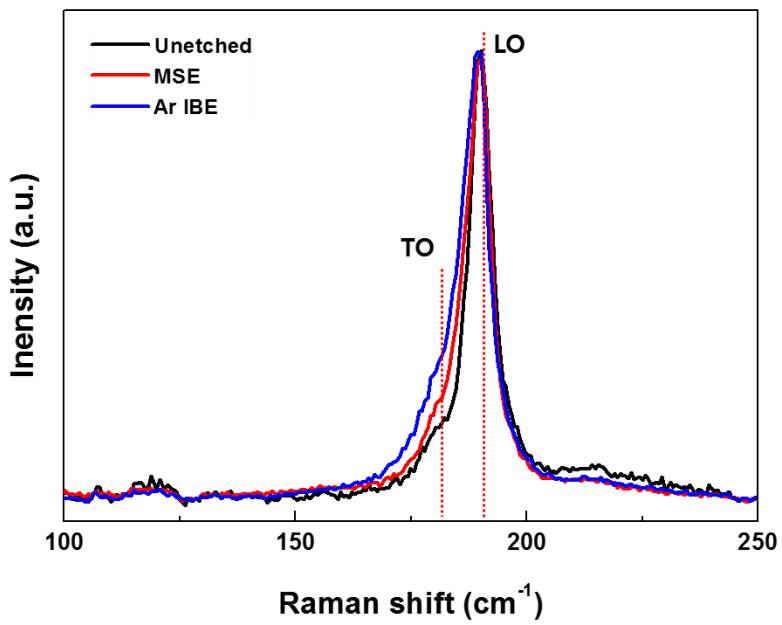


Fig. 5.7. Comparison of Raman spectrum obtained from etched surface using MSE with Ar IBE.

Fitted - LO peak	Ar IBE	Multi-step
Integrated area ratio (A_{TO}/A_{LO})	0.15	0.06
FWHM (cm^{-1})	7.11	5.71
Peak position (cm^{-1})	188.5	190

Table 5.1. Comparison of etching properties of MSE with IBE.

5.2 Growth temperature affecting passivation

5.2.1 Temperature dependence on trap density

Figure 5.8 shows the C-V characteristics of the MIS structures when the voltage was increased from – 20 V to 20 V. The characteristics were obtained from the structures for which the SiO₂ layers were deposited at different temperature ranging from 100 °C to 350 °C. The C-V characteristics were categorized into two groups, A and B. In the case of group A, the C-V curves changed gradually with increasing the deposition temperature.

Figure 5.9 represents the change of bulk trap density and interface trap density as a function of deposition temperature. As deposition temperature of SiO₂ increases from 100 to 250°C (as shown in the A region of the Fig. 5.8), flat band voltage shift, which is linear to fixed charges, and interface trap density decreased. But, the change of interface trap density is little in aspect of order. Relatively lower interface trap density of 2.0~2.1 x10¹² cm⁻² and bulk trap density of 1.7~2.3 x10¹¹ cm⁻², were observed from the sample deposited at 250 °C.

In the C-V curve, negative fixed charge results in changes of surface potential in InSb and this could induce inversion of the surface

from n-type to p-type. Then, the inversion layer could act as a leakage path in pn-junction. Also, interface traps help R-G, tunneling or surface diffusion occur easily and act as a leakage path. So we can conclude that 250 °C should be chosen as deposition temperature of SiO₂ for low interface traps and fixed charge SiO₂ layers.

However, as shown in the B region of Fig. 5.8, when the temperature was above 300 °C, the C-V characteristics began to breakdown. The failure cause of C-V characteristics is discussed in the next section.

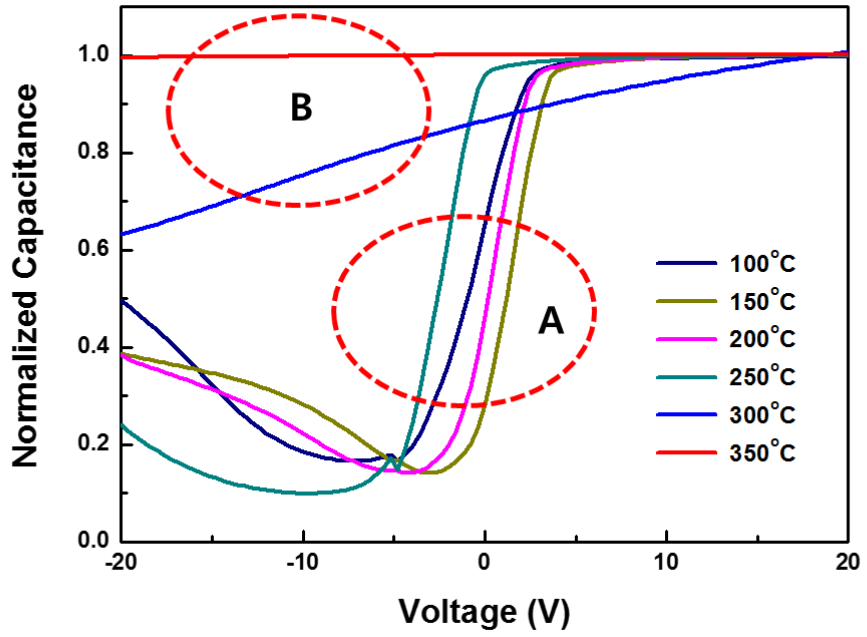


Fig. 5.8. C-V characteristics of Au/SiO₂/InSb MOS structures at frequency of 1 MHz.

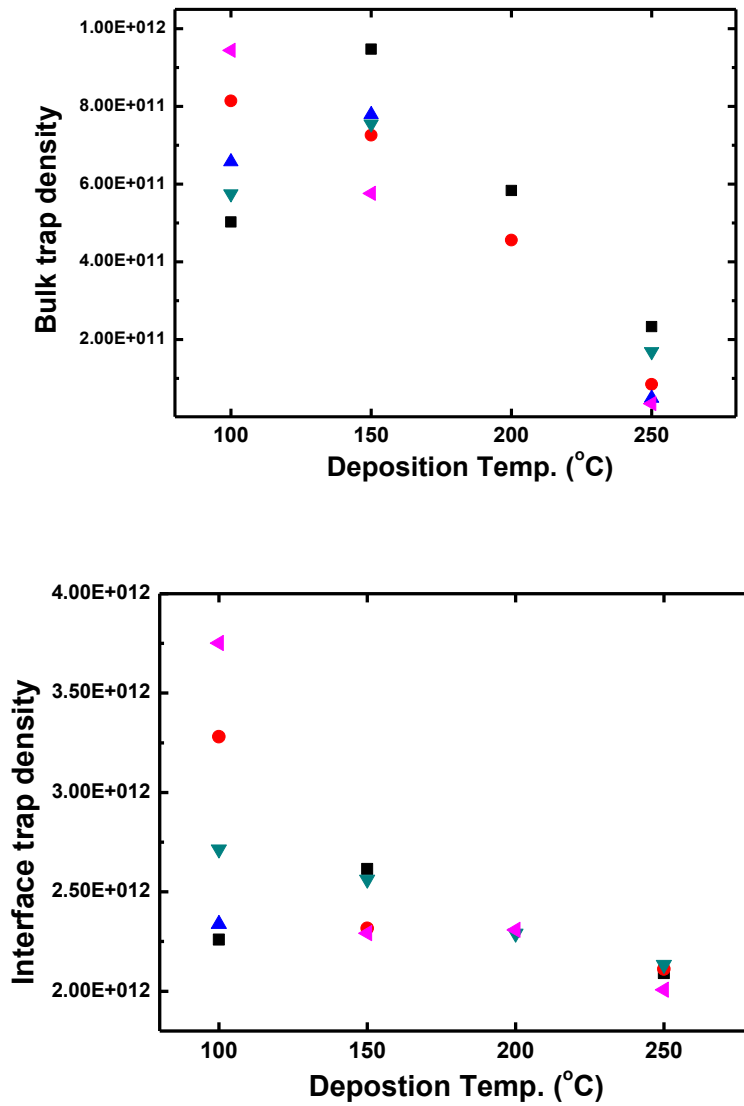


Fig. 5.9. Change of bulk trap density and interface trap density as a function of deposition temperature.

5.2.2 Failure cause of C-V characteristics

When the temperature was above 300 °C, the C-V characteristics began to change dramatically. The samples deposited at 300 °C, 350 °C had not normal C-V shape of metal-insulator-semiconductor (MIS) structure but normal C-V shape of metal-insulator-metal (MIM) structure that capacitance is proportional to voltage [9, 10, 11].

In order to investigate the cause of this structure change, Raman measurement was conducted. Raman spectra of the SiO₂-deposited InSb(100) surfaces are represented in Fig. 5.10. Two distinct peaks at 113 cm⁻¹ (TO mode) and 153 cm⁻¹ (LO mode) corresponding to elemental Sb were shown when the oxide layer was deposited above 300°C [12]. To show these peaks more clearly, the Raman spectra of the samples deposited at 300 and 350°C were shown separately in Fig. 5.11, respectively. It is observed that the intensity of the elemental Sb peaks is enhanced more significantly than those for InSb with increasing the temperature. This indicates that the Sb layers having metallic properties were formed due to the chemical reaction (eq. 4-1) of InSb with Sb₂O₃ [13].

As a result, the failure of C-V characteristics of the MIS structure deposited above 300 °C was originated from the formation of Sb phase because elemental Sb has metallic properties. The different band diagrams of MIS and MIM structure were shown in Fig. 5.12 (a) and (b). Work function of Sb and InSb is 4.6 eV and 4.59 eV, respectively. The difference of work function between two materials is about 0.01 eV. It is too small to act as a shotkey barrier, thus it is possible that elemental Sb makes an ohmic contact to InSb. As a result, the shape of C-V characteristics of MIS structure with SiO₂ layer deposited above 300 oC was changed to that of an MIM structure.

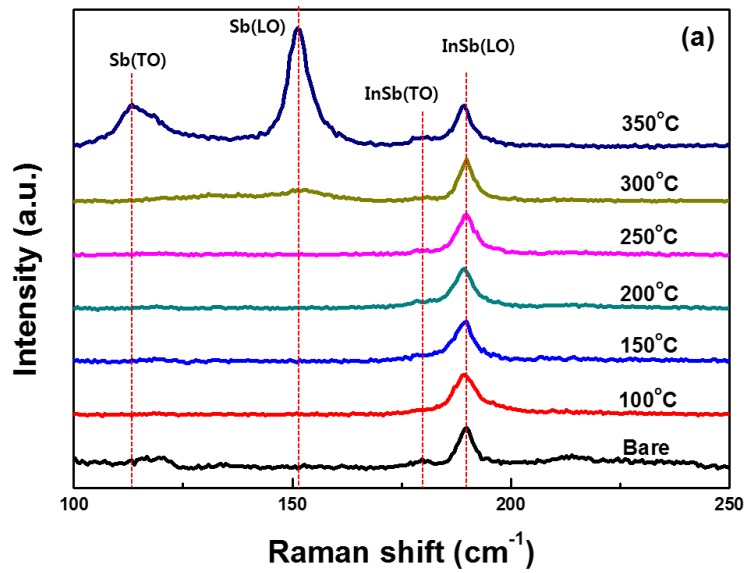


Fig. 5.10. Raman spectra for the SiO₂/InSb samples deposited at various temperature.

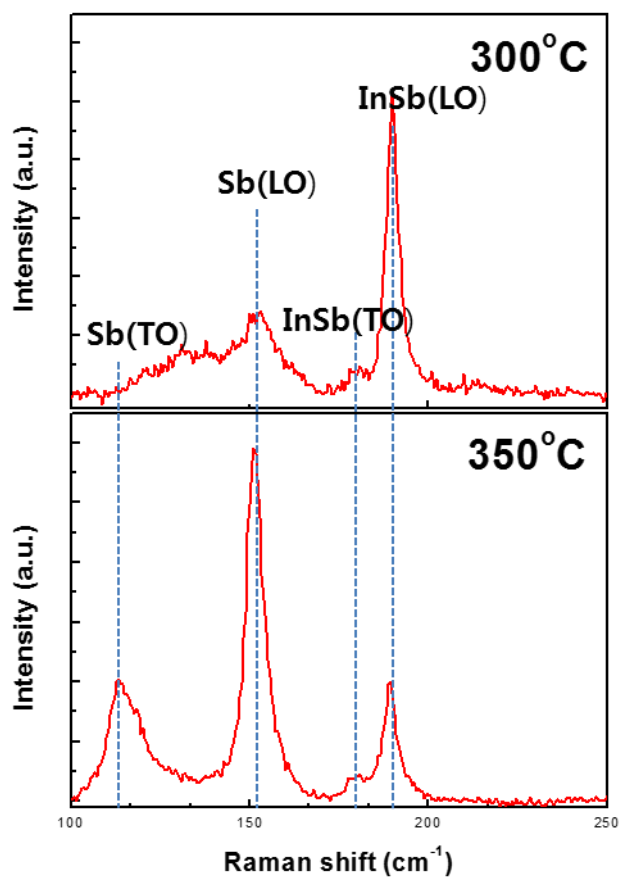
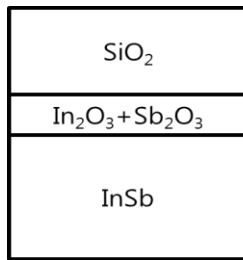
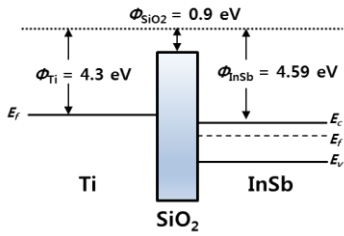


Fig. 5.11. Raman spectra of the sample deposited at 300°C and 350°C.

(a) MOS structure : Au/Ti/SiO₂/InSb



(b) MIM structure : Au/Ti/SiO₂/Sb/InSb

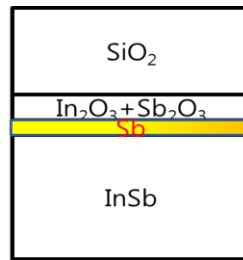
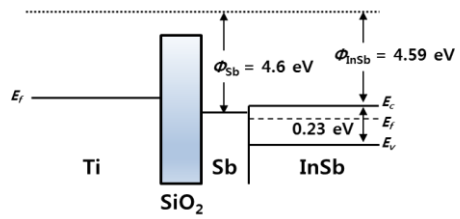


Fig. 5.12. Band diagram of (a) MIS structure: Ti/SiO₂/InSb and (b) MIM structure: Ti/SiO₂/Sb/InSb.

5.3 Summary

In this chapter, to reduce and prevent the defect generation during fabrication process, multi-step plasma etching process and low-temperature passivation process were studied.

In the section 5.1, to find the most effective etching method for the fabrication of InSb FPAs, comparative study of the conventional methods were conducted. It seemed reasonable to assume that, among the conventional methods, N₂ RIE could result in the best morphology of etched InSb surfaces. However, due to the extremely slow etching speed of N₂ RIE, it is hard to apply in the fabrication process. As an alternative, the MSE process combining both techniques was developed to solve these problems. In comparison with Ar IBE method, it was demonstrated that MSE process is a very suitable method for InSb with smooth surface at moderate etch rates and less defect induced by plasma.

In the section 5.2, the effect of deposition temperature of SiO₂ passivation layer on the C-V characteristics was investigated. It was proven that Sb phase was induced by thermal energy and chemical reaction and it can act as a critical defect in the case of InSb devices. Due

to the metallic Sb layer between SiO₂ and InSb, the C-V characteristic of MIS structure with SiO₂ layer deposited above 300 °C was changed to that of MIM structure. This results indicates that the fabrication process of SiO₂ deposited MIS device should be done at lower temperature than 300°C to suppress the formation of elemental Sb phase.

5.4 References

- [1] Rogalski, A., “Infrared Detectors 2nd edition”, CRC Press, Taylor and Francis Group, 309-352 (2011).
- [2] Melville, D. L., Simmons, J. G., and Thomson, D. A., “Identification of volatile products in low pressure hydrocarbon electron cyclotron resonance reactive ion beam etching of InP and GaAs,” J. Vac. Sic. Technol. **B** 11(6), 2038-2045 (1993).
- [3] Vawter, G. A. and Vendt, J. R., “Chlorine reactive ion beam etching of InSb and InAs_{0.15}Sb_{0.85}/InSb strained layer superlattices,” Appl. Phys. Lett. **58**, 289 (1991).
- [4] Pearton, S. J., Chakrabarti, U. K., Hobson, W. S. and Perly, A. P., “Cl₂ and SiCl₄ reactive ion etching of In-based III-V semiconductors,” J. Electrochem. Soc. Vol. 137, issue 10, p3188-3202 (1990).
- [5] Bharadwaj, L. M., Bonhomme, P., Faure, J., Balossier, G. and Bajpai, R. P., “Chemically assisted ion beam etching of InP and InSb using reactive flux of iodine and Ar⁺ beam,” J. Vac. Sci. Technol. **B** **9**, 1440 (1991).

- [6] Frost, F., Schindler, A., and Bigl, F., "Reactive ion beam etching of InSb and InAs with ultrasmooth surfaces," *Semicond. Sci. Technol.* **13**, 523-527 (1998).
- [7] Seok, C., Choi, M., Park, S., Jung, J., Park, Y., Yang, I. S., and Yoon, E., *ECS Solid State Letters*, 3(3), p27-29 (2014). I. I. Bloom, Y. Nemirovsky, *IEEE Trans. Electron Devices* **40**, 309 (1993).
- [8] A. Rogalski, *Prog Quantum Electron* **27**, 59 (2003).
- [9] J. Woo, Y. Chun, Y. Joo, and C. Kim, *Appl. Phys. Lett.* **100**, 081101 (2012).
- [10] S. J. Kim, M. Li, S. Ding, C. Zhu, M. B. Yu, B. Narayanan, A. Chin, and D. Kwong, *IEEE Electron Device Lett.*, **Vol. 25**, No. 8 (2004).
- [11] S. J. Kim, B. J. Cho, M. Li, S. Ding, M. Yu, C. Zhu, A. Chin, and D. Kwong, *Symposium on VLSI Technology Digest of Technical Papers*, p218-219 (2004).
- [12] W. Richter and J. F. McGilp, *Phil. Trans. R. Soc. Lond.* **A 344**, p453-467 (1993).
- [13] J. Lee, S. Park, J. Kim, C. Yang, S. Kim, C. Seok, J. Park, and E. Yoon, *Thin Solid Films* **520**, 5382-5385 (2012).

Chapter 6.

Conclusion

6.1 Summary of results

The objective of this thesis is to find the answers about both “What kind of defect can be generated by plasma and heat” and “How to reduce or prevent it”. To achieve this objective, the research has been focused in two way, one is on how to measure the surface defect for investigating what kind of defect are existing and the other is on how to reduce and prevent the defect generation during fabrication process.

In the chapter 3, plasma-induced defect on InSb surface was studied. To analyze the fine defect on the surface, Raman method was applied to our research. By measuring the degree of enhancement of TO scattering, theoretically it has to be forbidden in the spectra of (100) plane according to Raman selection rule, the information related with plasma-induced defect and RF power dependence on defect generation could be measured effectively. Furthermore, it was demonstrated that the origin of enhanced TO phonon scattering is plasma-induced defects such as Sb vacancy due to the preferential loss of Sb atoms.

In the chapter 4, thermally generated defect on InSb surface was studied. By the *in-situ* monitoring using Raman spectroscopy and 2-D peak mapping of InSb surface, antimony segregation was clearly examined. Due to the thermally generated chemical reaction of InSb with Sb_2O_3 during annealing process, it was proved that Sb phase was segregated on the surface at high temperature above 400°C or at relative lower temperature with long-annealing time. It was proved that temperature and time are strong factors affecting the segregation reaction. Moreover, it was shown that Segregated Sb phase was existed between native oxides and InSb substrate and the thickness of Sb phase was about 5 nm via AES depth-profile. Thus, to avoid the segregation, the annealing temperature have to be kept below 250°C during fabrication process.

In the chapter 5, to reduce and prevent the defect generation during fabrication process, multi-step plasma etching process and low-temperature passivation process were studied. In the first section, to overcome the limitation of conventional plasma-etching method, the MSE process combining both Ar IBE and N_2 RIE techniques was developed to solve these problems. In comparison with conventional

method, it was demonstrated that MSE process is a very effective method reducing the plasma-induced defect for the fabrication of InSb FPAs.

In the next section, it was proven that Sb phase was induced by thermal energy and chemical reaction and it can act as a critical defect in the case of InSb devices. Due to the metallic Sb layer between SiO₂ and InSb, the C-V characteristic was failed. This results indicates that the fabrication process of SiO₂ deposited MIS device should be done at lower temperature than 300°C to suppress the formation of elemental Sb phase.

In conclusion, it was demonstrated that defects having a strong relation with preferential loss of Sb atom were generated by bombarded ions during plasma etching process and it could be measured effectively by using Raman spectroscopy. Especially we could find that the enhancement of forbidden TO scattering was originated from the loss of Sb. Moreover, it was proven that excess Sb atom were segregated on the surface above the critical temperature of 400°C and this Sb phase made the device performance degrade. The plasma-induced defect and thermal reaction of Sb segregation depends on the RF power and the temperature

and time, respectively. Thus, to reduce these defects, MSE process and low-temperature passivation process were required.

6.2 Detectivity enhancement

In this thesis, the surface defect induced by plasma and thermal energy was investigated. Based on the results obtained from this study, the fabrication process was optimized. To reduce the plasma-induced defect, MSE was adopted instead of Ar ion beam etching. For minimizing the interface trap and bulk trap density of SiO₂ passivation layer, low-temperature passivation at 250°C was performed. Moreover, to prevent the segregation of antimony during annealing process, all fabrication process were conducted below the temperature of 250°C, except epitaxial growth of InSb.

As a result, we can enhance the R₀A value of InSb photodiode fabricated by applying the optimized conditions from $2 \times 10^3 \text{ } \Omega\text{cm}^2$ to $9.3 \times 10^3 \text{ } \Omega\text{cm}^2$.

Appendix. I

Catalyst-free InSb Nanocrystals growth

A.1 Introduction

Indium antimonide (InSb) has attracted considerable research attention as a next generation channel material due to many advantages in comparison with Si, such as the high electron mobility ($80000 \text{ cm}^2/\text{Vs}$) and the narrow energy band gap (0.18 eV). For compound semiconductor MOSFET devices, the epitaxial growth of InSb on other materials such as GaAs or Si has been successfully used to form the active region. However, layer-by-layer growth of highly crystalline InSb thin films on GaAs is extremely difficult, because the lattice mismatch of 14.6% between InSb and GaAs generates misfit strain and immiscibility problems. Since this lattice mismatch is larger than that of the pseudo-morphic growth limit of 10-12% [1,2], theoretically calculated, the

epitaxial growth of InSb on GaAs generally begins in the Volmer-Weber mode, i.e., three-dimensional island growth.

Interestingly, however, due to the highly lattice-mismatched axial and radial heterostructures, considering that as a form of nano particle, nano-materials have different electronic, mechanical and optical properties compared to that of bulk materials. Especially, InSb nanocrystals (NCs) are viewed as an alternative materials to conventional semiconductors and it has been studied to find new applications for the devices. In this sense, extensive research efforts have been devoted to the voted to the studies and developments of III-V semiconductor nano-materials and recent progress in nano-heteroepitaxy has enabled high-crystallinity and low-defect III-V NCs to form on largely lattice-mismatched substrates. [3,4]

InSb NCs have been grown using Au-catalyzed metal-organic chemical vapor deposition (CVD). [5-8] Most of all reported epitaxial

methods were based on the growth mechanism that use metal catalyst and initially formed InSb segment as a seed layer to assist the InSb NC formation. However, there has been problems of Au atom contamination in the NCs using Au-catalyzed method. This Au atoms act as a recombination centers in III-V semiconducting materials. [9] Moreover, these atoms can reduce the minority carrier lifetime and increase the scattering, therefore it can cause the degradation of device performance. Thus, due to this reason, catalyst-free epitaxy of InSb NCs on GaAs has a great importance. [10]

In this work, InSb NCs were directly grown on GaAs(100) substrate without any metal-catalyst and InSb segment using low pressure-MOCVD in the range from at 435°C and 465°C, and then the effect of V/III ratio and temperature on the growth and coalescence of NCs were investigated via X-ray diffraction (XRD), atomic force microscopy (AFM) and scanning electron microscope (SEM).

A.2 Experimental Details

InSb NCs were grown on GaAs (100) substrates with a low-pressure (76 torr) MOCVD, using trimethyl-indium (TMIn) and trimethyl-antimony (TMSb) as precursors. Fig. A. 1 shows the schematic of equipment and growth procedure using in this experiment. The epi-ready GaAs substrates are thermally cleaned under AsH₃ ambient at 710°C for 5 minutes to eliminate native oxides on the GaAs surfaces. The growth temperature in this study is limited by the cracking temperature of TMSb (430°C) at low-temperature side and the melting temperature of InSb (525°C) at high-temperature side. After growth, the samples were cooled down under Sb overpressure to prevent InSb desorption. The resulting structures are studied by SEM and AFM to determine the InSb NCs formation and morphology. Further structural properties and chemical analysis were examined by XRD and energy dispersive X-ray spectroscopy (EDX).

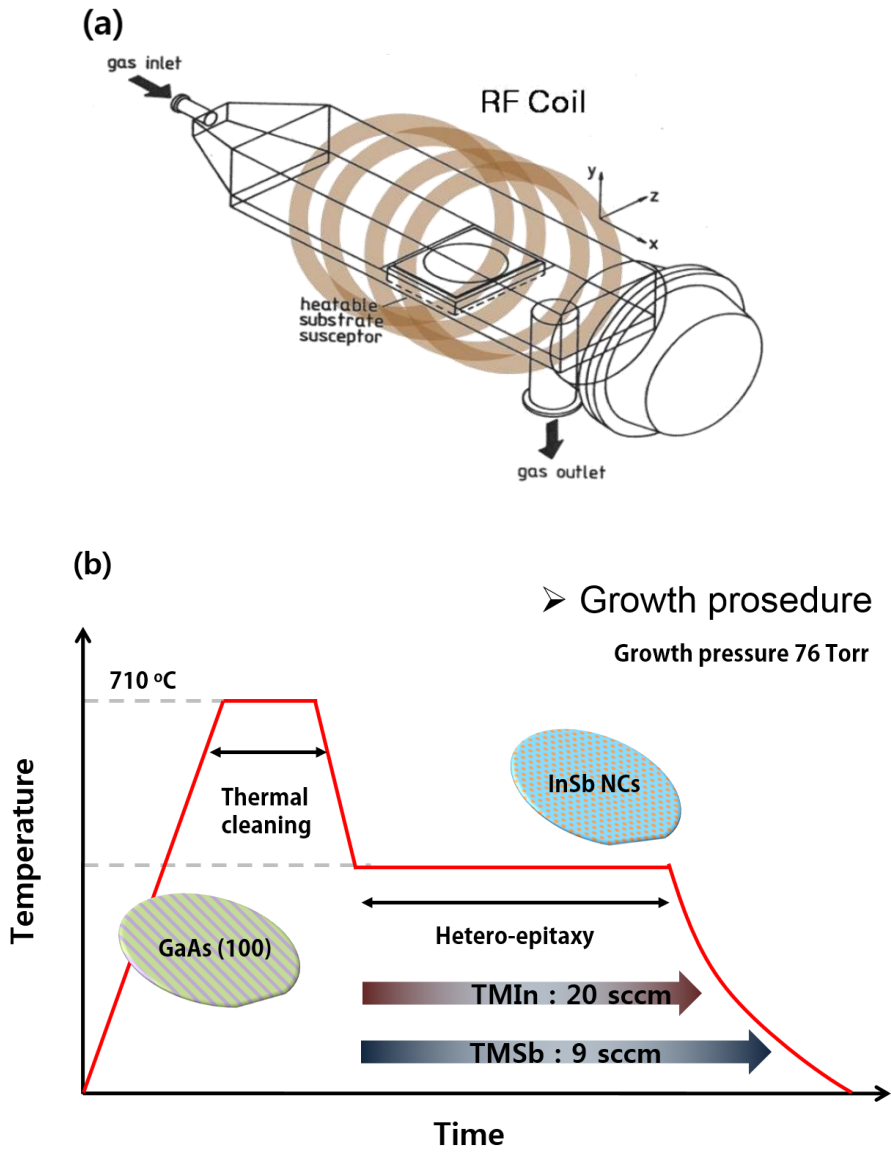


Fig. A. 1. (a) Schematic of MOCVD equipment and (b) process flow of InSb NCs epitaxial growth by using LP-MOCVD.

A.3 Growth of InSb NCs

Figure A.2 represents the XRD data obtained from GaAs(100) substrate covered by epi-grown InSb NCs. The distinct peak of InSb (400) indicated that the crystalline InSb were grown on GaAs by MOCVD.

Figure A.3 shows the morphologies of directly grown InSb NCs on GaAs (100) substrates. Due to the large lattice-mismatch, the island growth mode was dominate, thus formed InSb NCs had a clear facets originated from the different surface energies.

Figure A.4 indicates the facets index of InSb NC. [11] The surface energy of {111} plane is larger than that of {100} plane. Thus, added Sb atoms tended to migrate into sidewall with {111} plane and it resulted in the distinct facet formation.

The direct growth of InSb NCs by MOCVD are extremely sensitive to the growth environments including the V/III ratio and the growth temperature. The effects of V/III ratio on NCs growth was clearly shown

in Figure A. 5. When the V/III ratio was larger than 10, indium (In) droplets were not observed due to the change into InSb NCs satisfying atomic stoichiometry.

Figure A. 6 illustrates the speculated growth mechanism of the InSb NC. Dissolved Sb atoms in the In droplet diffuse to the interface region of In and InSb. Then InSb epitaxially crystallized at the interface. Thus at high V/III ratio, In droplets could be fully transformed to InSb NCs.

Moreover, the size and density of NCs strongly depended on the growth temperature as shown in Fig. A. 7 and Fig. A. 8. As a results, with the temperature increasing, the average size of InSb NCs also increased, on the other hand, the density of NCs decreased. It was because the migration of atoms and the coalescence of NCs were facilitated at high temperature.

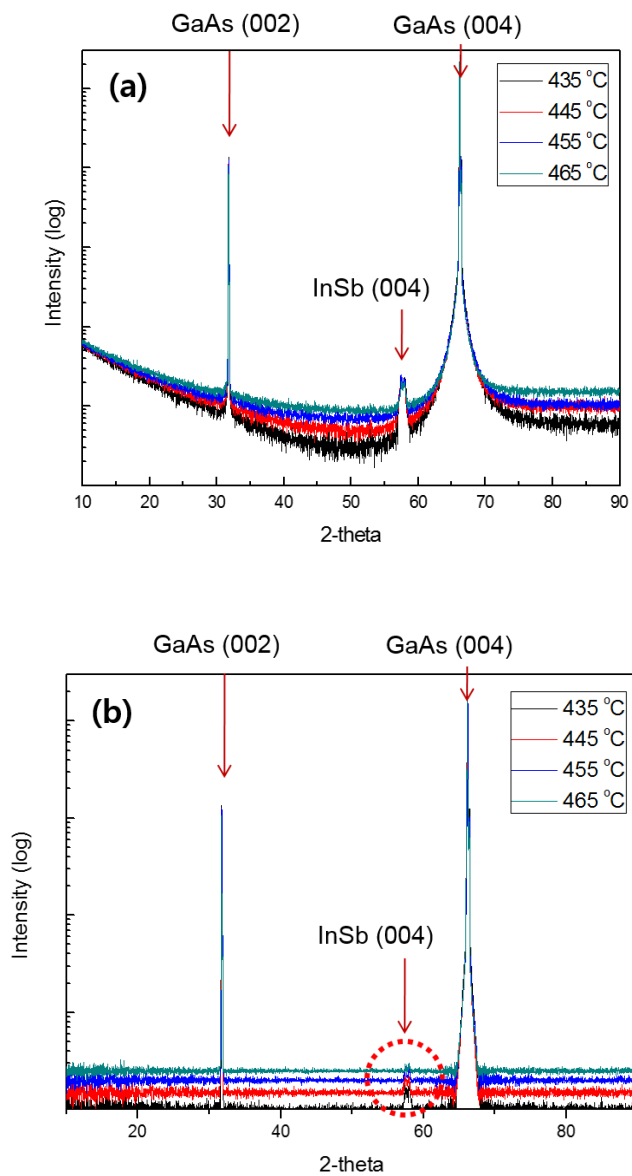


Fig. A. 2. XRD results of epi-grown InSb NCs on GaAs (a) without elimination and (b) with elimination of background signals.

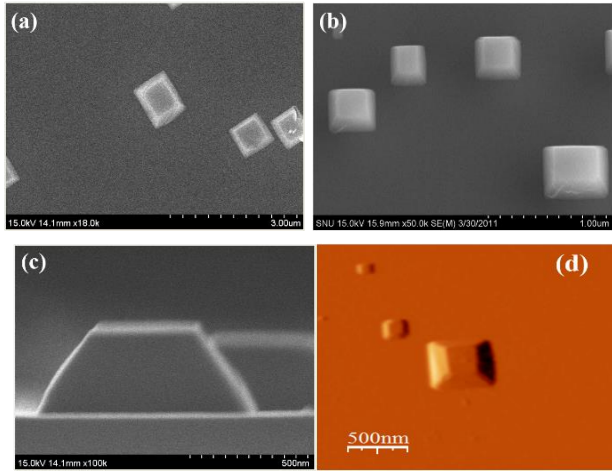


Fig. A. 3. (a) Plane-view SEM image of InSb NCs. (b) Tilted-view SEM image of InSb NCs. (c) Cross-sectional SEM image of InSb NCs. (d) AFM image of InSb NCs.

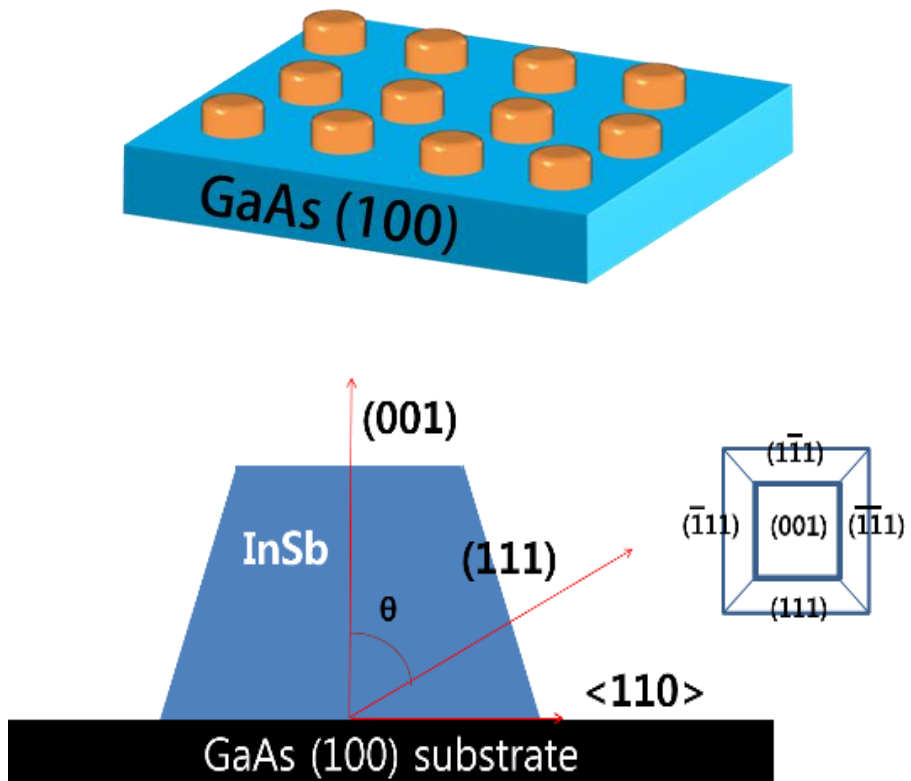


Fig. A. 4. Schematic explanation of catalyst-free grown InSb nanocrystal on GaAs substrate with facet index.

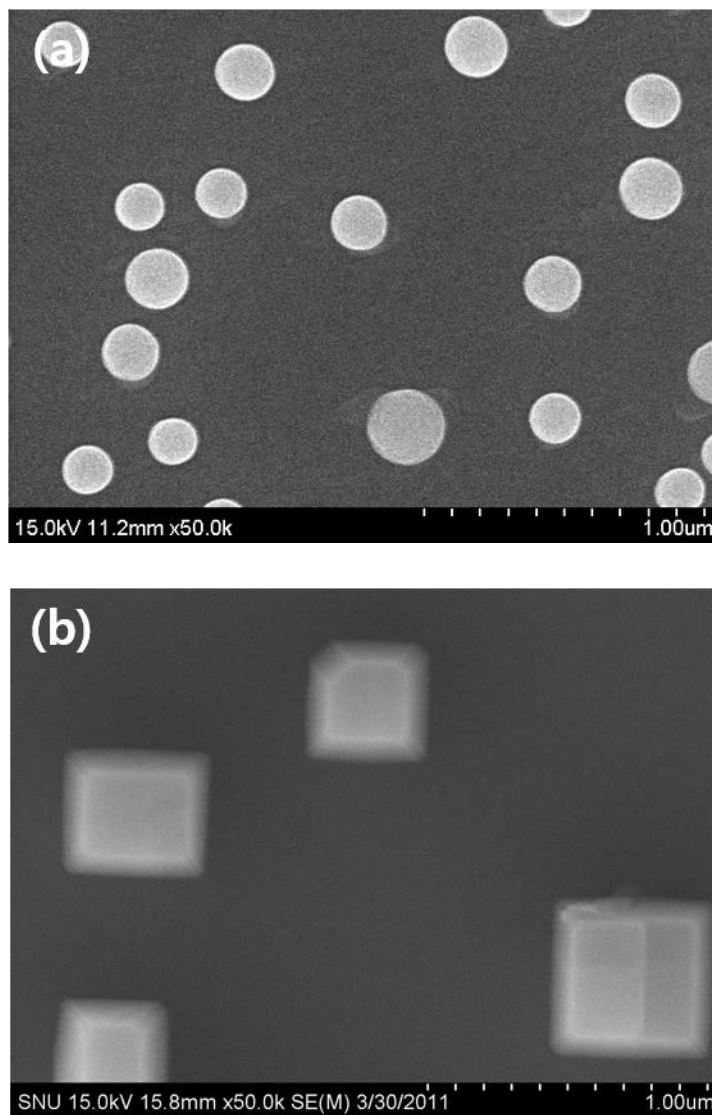


Fig. A. 5. Plane-view SEM images of InSb NCs grown at 465°C using a condition of (a) V/III ratio = 8 and (b) V/III ratio = 10.

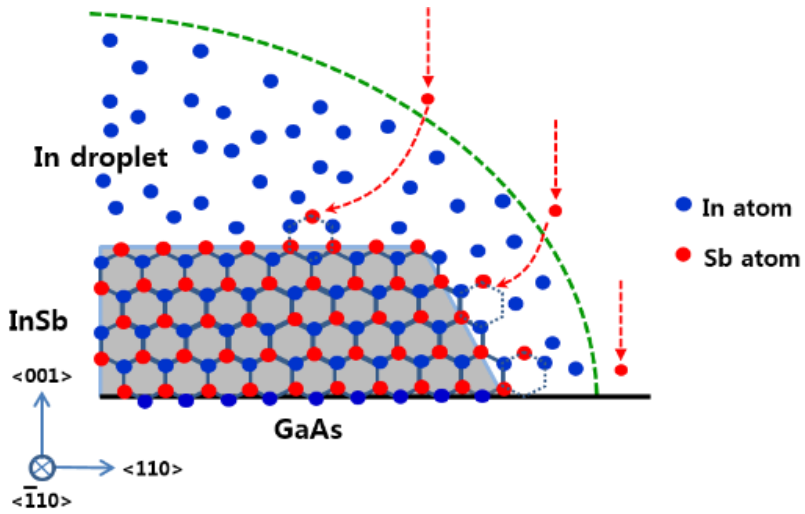


Fig. A. 6. Growth mechanism of InSb nanocrystals with cross-sectional view along $\langle 110 \rangle$ axis.

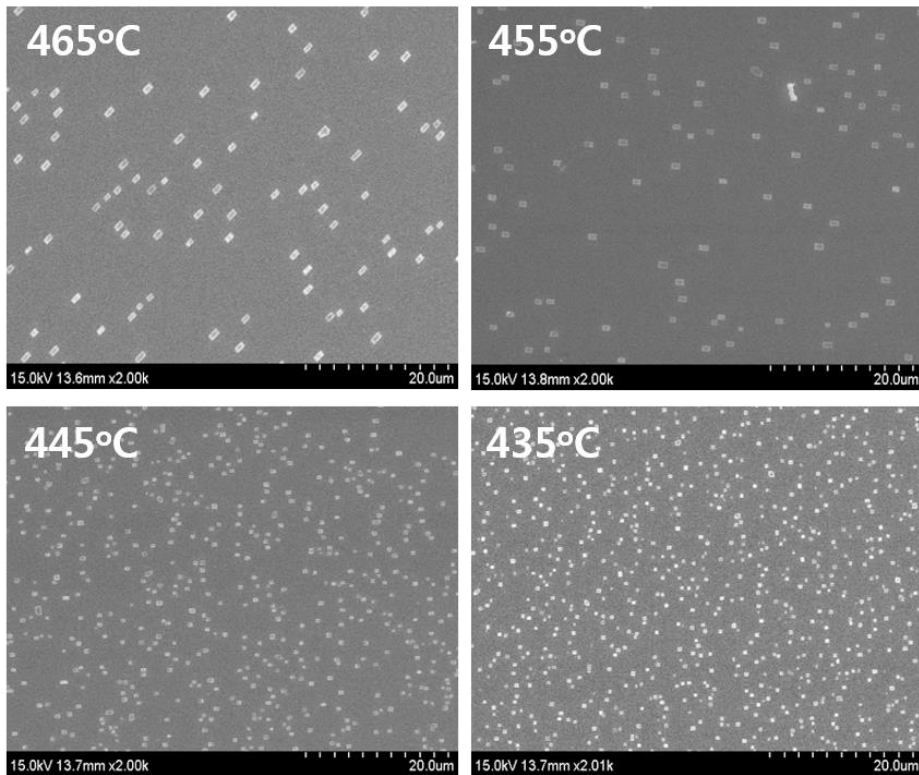


Fig. A. 7. SEM images of epi-grown InSb NCs on GaAs substrate at various growth temperature.

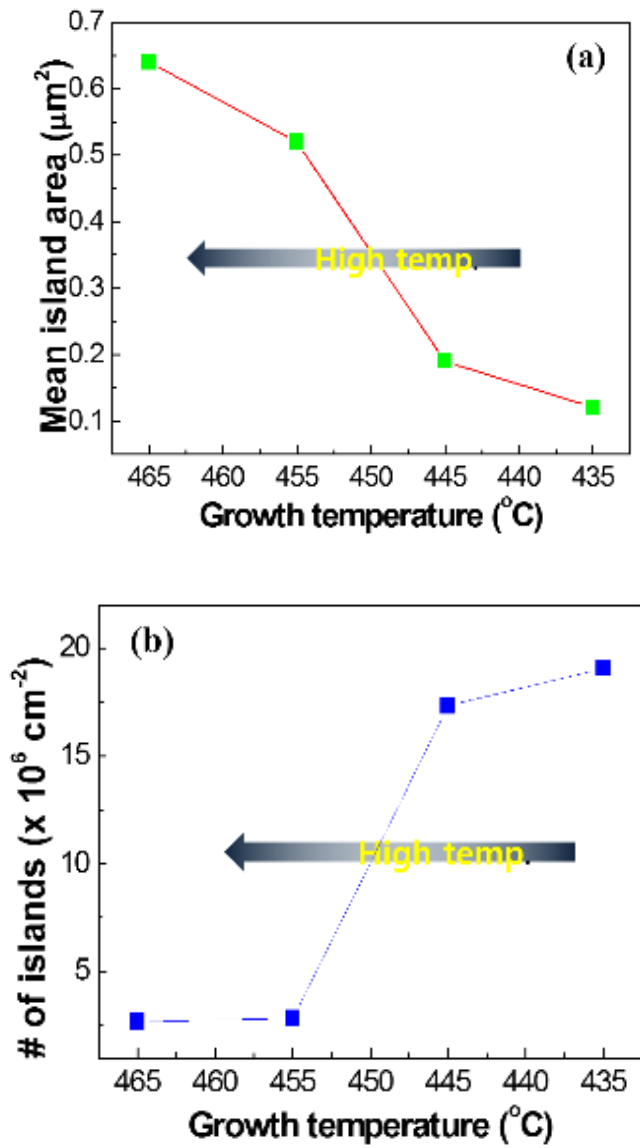


Fig. A. 8. Parameter changes as a function of deposition temperature (a) average size and (b) average density of InSb NCs.

A.4 Conclusion

In this work, the growth conditions for InSb NCs directly on GaAs (100) substrates has been investigated. From the observed results of NCs, we could show how the density and the average size of InSb NCs can be controlled by the temperature and V/III ratios. As the growth temperature increased from 435°C to 465°C, the density of InSb NCs decreased from 1.9×10^7 to 2.5×10^6 cm⁻². It was also observed that at the higher temperature the number of gigantic InSb NCs increased significantly and as a result the average size of NC increased. This phenomenon could be explained by the enhanced coalescence of NCs at the higher temperature. Furthermore, using lower V/III ratios below 10, In droplet formed and it resulted in catalyst-free NC growth.

Interestingly, gigantic InSb NCs as well as unit NCs were observed on the epi-grown samples at various growth temperature. As shown Fig. A. 9, the size of gigantic NC was about 10x15 μ m and it has

asymmetric shape. EDX results in Fig. A. 10 clearly indicated that the gigantic NC was also InSb. We speculated that the coalescence of unit NCs made these gigantic crystals, however the reason why the coalescence occurred only a small part of surface could not be proved yet. Further research on this is required and the advanced research will be addressed.

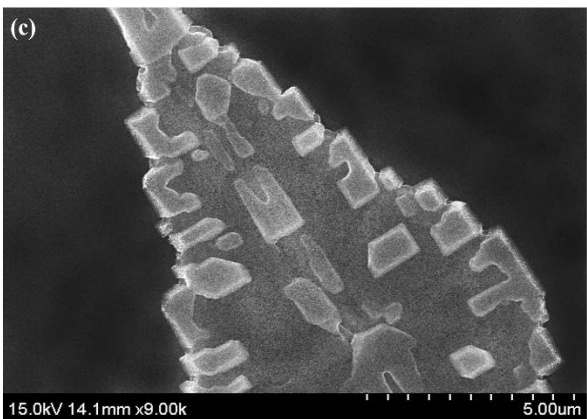
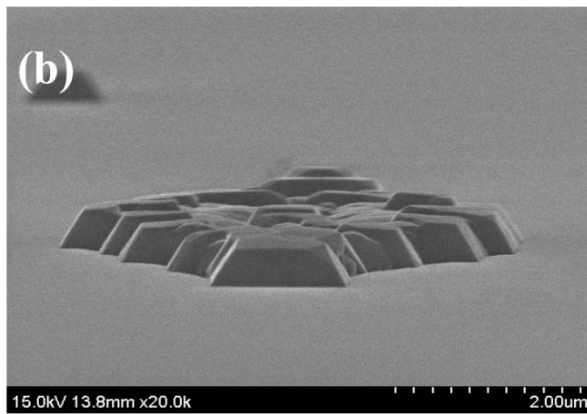
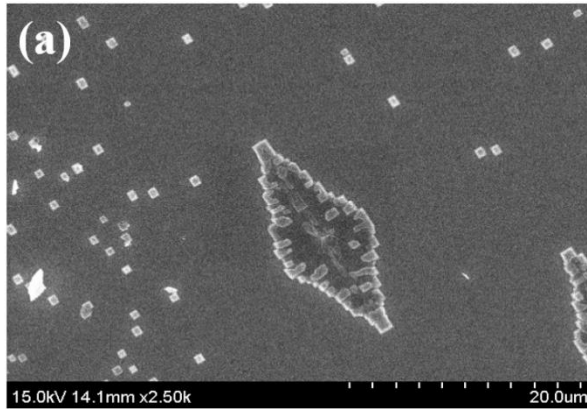


Fig. A. 9. SEM image of gigantic InSb NC.

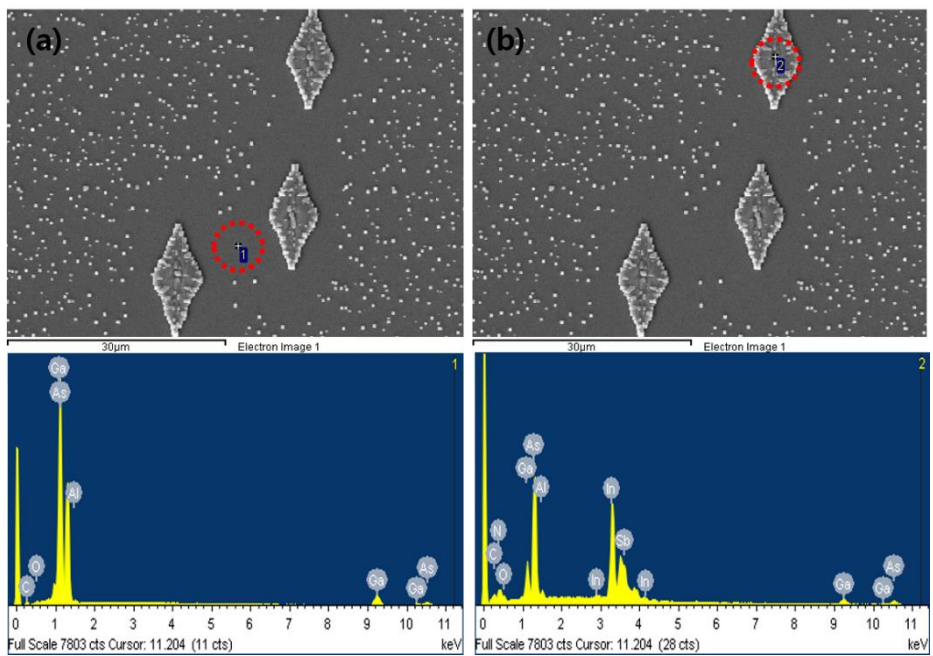


Fig. A. 10. SEM image and EDX data of GaAs substrate covered by gigantic InSb NCs

A.5 References

- [1] I. Daruka and A. L. Barabasi, *Phys. Rev. Lett.* 79, 3708 (1997).
- [2] G. B. Stringfellow, *Crystal Growth 2nd ed.*, p.211 (1980).
- [3] K. Tomioka, M. Yoshimura, and T. Fukui, *Nature* 488, 189 (2012).
- [4] X. Y. Bao, C. Soci, D. Susac, J. Bratvold, D. P. R. Aplin, W. Wei, C. Y. Chen, S. A. Dayet, K. L. Kavanagh, and D. Wang, *Nano Lett.* 8, 3755 (2008).
- [5] P. Caroff, J. B. Wagner, K. A. Dich, H. A. Nilsson, M. Jeppsson, K. Deppert, L. Samuelson, L. R. Wallenberg, L. E. Wernersson, *Small* 4, 878 (2008).
- [6] S. R. Plissard, D. R. Slapak, M. A. Verheijen, M. Hocevar, G. W. G. Immink, I. van Weperen, S. N. Perge, S. M. Frolov, L. P. Kouwenhoven, E. P. A. M. Bakkers, *Nano Lett.* 12, 1794 (2012).
- [7] X. Yang, G. Wang, P. Slattery, J. Z. Zhang, Y. Li, *Crystal Growth Design* 10, 2479 (2010).
- [8] H. D. Park, S. M. Prokes, M. E. Twigg, Y. Ding, Z. L. Wang, *J. Crystal Growth* 204, 399 (2007).
- [9] J. E. Allen, E. R. Hemesath, D. E. Perea, J. L. Falk, Z. Y. Li, F. Yin., M. H. Gass, P. Wang, A. L. Bleloch, R. E. Palmer, L. J.

Lauhon, *Nat. Nanotechnol.* 3, 169 (2008).

[10]A. Lin, J. N. Shapiro, H. Eisele, and D. L. Huffaker, *Adv. Funct. Mater.* 24, 4311 (2014).

[11]H. D. Barber, E. L. Heasell, *J. Electrochem. Soc.* 114, 6, 635 (1967).

국 문 초 록

이 연구의 목표는 소자 제작 공정 과정에서 인듐 안티모나이드에 인가되는 플라즈마와 열에 의해 각각 어떠한 표면 결함이 발생하는지 밝히고, 이를 줄이는 방법을 제시하는 것에 있다.

먼저 공정 중에 인가되는 플라즈마에 의해 발생하는 표면 결함의 종류를 확인하기 위하여, 라만분석법이 적용되었다. 그 결과, 라만선택율에 의하면 (100)면에서 보이지 않아야 하는 TO 포논이 플라즈마 식각된 표면에서 관찰되었고, 그 세기는 인가되는 플라즈마의 RF power 에 비례하여 증가함이 관찰되었다. 이는 기존에 보고된 가설과는 달리, 표면거칠기에 의한 것이 아닌 플라즈마에 의해 인듐 안티모나이드 표면에 생성되는 안티모니 공공에 의한 것임을 규명하였다.

또한 공정 중에 노출되는 열에너지에 의해 표면에 안티모니의 석출상이 생성됨을 확인하였다. In-situ 라만분석 및 안티모니의 LO phonon 을 맵핑하여, 450도 이상의 온도부터 안티모니 석출이 부분적으로 발생하기 시작하여,

500도에서 표면 전체에 형성됨을 규명하였고, 그 석출과정이 Grain 성장과 비슷한 모습으로 진행됨을 처음으로 증명하였다.

이러한 플라즈마에 의한 안티모니 공공 결함 발생 및 열에 의한 안티모니 석출상 생성을 억제하기 위하여, 먼저 아르곤 플라즈마 식각과 질소 플라즈마 식각을 단계적으로 수행하는 다중 식각 공정을 고안하여 적용하였고, 그 결과, 아르곤 플라즈마 에칭과 비교했을 때, 에칭 후 표면거칠기 값이 1.8129 nm 에서 0.1415 nm 로 크게 감소하였고, 라만 스펙트럼 상의 TO 포논과 LO 포논의 세기비율이 0.15에서 0.06으로 감소하므로, 이를 통해 플라즈마에 의한 안티모니 결함 발생도 크게 줄일 수 있음을 확인하였다. 또한, 표면부동화 과정에서 SiO₂의 증착온도가 250도 일 때, 표면 결함을 최소화할 수 있으며, 300도 이상에서는 안티모니가 석출되어 그 특성이 크게 변화하므로 지양해야 함을 규명하였다.

이러한 표면 결함 발생 및 억제 연구를 실제 소자 제작 공정에 응용하여, 암전류를 감소시켜 R_{0A} 값을 향상시킬 수 있었다. 본 연구를 통해 얻어진 결과는 향후 안티모니 계열의 다른 화합물 반도체에도 효과적으로 적용되어, 소자 개발에 이바지 할 수 있을 것으로 예상된다.

Keywords:

인듐안티모나이드(InSb), 적외선 검출기, 압전류, 표면결합,
라만분광법, 플라즈마 유도결합, 안티모니(Sb) 석출

학 번: 2008-20652

PUBLICATION LIST

Papers:

International journal:

- 1) **C. Seok**, M. Choi, S. Park, J. Jung, Y. Park, I. Yang, E. Yoon,
“Raman spectroscopy of the damages induced by Ar-ion beam etching of InSb(100) surface”, ECS Solid State Letters, Vol. 3, Issue 3, p27-29 (2014).
- 2) **C. Seok**, M. Choi, H. Park, S. Park, Y. Park, I. Yang, E. Yoon,
“Annealing effect on InSb surface via in-situ Raman spectroscopy”, in preparation.
- 3) **C. Seok**, M. Choi, S. Park, H. Park, Y. Park, I. Yang, E. Yoon,
“Relation between enhancement of forbidden TO phonon and etching-induced damage on InSb(100) surface via Raman spectroscopy”, in preparation.
- 4) S. Park, J. Jung, **C. Seok**, K. Shin, S. Park, Y. Nanishi, Y. Park, E. Yoon, “Effects of TMSb overpressure on InSb surface morphology for InSb epitaxial growth using low pressure

metalorganic chemical vapor deposition”, Journal of Crystal Growth, accepted (2013).

- 5) J. Lee, S. Park, J. Kim, C. Yang, S. Kim, **C. Seok**, J. Park, E. Yoon, “Comparative analysis of oxide phase formation and its effects on electrical properties of SiO₂/InSb metal-oxide-semiconductor structures”, Thin Solid Films, 520, 16, 5382 (2012).

Conference proceedings:

- 1) **C. Seok**, S. Kim, J. Lee, S. Park, Y. Park, and E. Yoon, “Analysis of failure of C-V characteristics of MIS structure with SiO₂ passivation layer deposited on InSb substrate via Raman spectroscopy”, *MRS Proceedings*, **1670** (2014).
- 2) **C. Seok**, M. Choi, I. Yang, S. Park, Y. Park, and E. Yoon, “Multi-step plasma etching process for development of highly photosensitive InSb mid-IR FPAs”, Proceedings of SPIE, **9070** (2014).
- 3) J. Lee, J. Woo, S. Park, J. Kim, C. Yang, S. Kim, **C. Seok**, K.

Lee, J. Park, M. Han, K. Seo, and E. Yoon, “Enhancement of interface properties between passivation layer and InSb by using remote PECVD”, *AIP Conference Proceedings*, **1399**, 105 (2011).

Presentation

International conference:

- 1) **C. Seok**, S. Kim, J. Lee, S. Park, H. Park, Y. Park, and E. Yoon, “Analysis for degradation cause of SiO₂ passivation layer deposited on InSb using PECVD”, The 5th International Conference on Microelectronics and Plasma Technology (ICMAP 2014), 2014.07.10, GSCO, Gunsan, Korea.
- 2) **C. Seok**, S. Lee, H. Park, S. Park, Y. Park, and E. Yoon, “Epitaxial growth and coalescence of InSb nano crystals on GaAs substrate using MOCVD”, The 12th International Nanotech Symposium & Nano-Convergence Expo (Nano Korea 2014), 2014.07.04, COEX, Seoul, Korea.
- 3) **C. Seok**, M. Choi, J. Jung, S. Park, Y. Park, I. Yang, E. Yoon,

“Multi-step plasma etching process for the development of highly detective InSb mid-IR sensor arrays”, SPIE DSS (Defense, Sensing and Security), 2014.05.06, Baltimore convention center, -Baltimore, U.S.

- 4) **C. Seok**, M. Choi, S. Park, J. Jung, Y. Park, I. Yang, and E. Yoon, “Ion beam etching induced damages on InSb surfaces studied by resonant Raman spectroscopy”, MRS (Material Research Society) Spring, 2014.04.23, Moscone west convention center, San Francisco, U.S.
- 5) **C. Seok**, M. Choi, J. Jung, S. Park, Y. Park, I. Yang, E. Yoon, “Multi-step plasma etching process for InSb photodiodes to minimize plasma-induced damages”, The 8th International Conference on Advanced Materials and Devices (ICAMD 2013), 2013.12.11, Ramada hotel, Jeju, Korea.
- 6) S. Park, J. Jung, S. Park, **C. Seok**, K. Shin, Y. Park, Y. Nanishi, and E. Yoon, “Effects of TMSb overpressur on InSb surface morphologies during a thermal cleaning process by low pressure metal organic chemical vapor deposition”, The 17th International Conference on Crystal Growth and Epitaxy (ICCGE-17),

2013.08.16, Univ. of Barsaw, Barsaw, Poland.

- 7) **C. Seok**, S. Park, J. Jung, Y. Park, and E. Yoon, “Ion beam induced structural damages on InSb surface studied by Raman spectroscopy”, The 16th International Symposium on the Physics of Semiconductors and Applications (ISPSA 2013), 2013.07.03, Ramada hotel, Jeju, Korea..
- 8) S. Park, S. Park, **C. Seok**, S. Kim, and E. Yoon, “Effects of deposition temperatures on the chemical species formation at the interfaces of Si₃N₄/InSb structures fabricated by plasma enhanced chemical vapor deposition”, The 4th International Symposium on Advanced Plasma Science and its Application for Nitrides and Nanomaterials (ISPlasma 2012), 2012.03.07, Chubu Univ., Aichi, Japan.
- 9) S. Park, J. Lee, J. Kim, S. Kim, **C. Seok**, C. Yang, J. Park, and E. Yoon, “The analysis of interface property between dielectric layer (Si₃N₄, SiO₂) and InSb for infrared photo-detector application”, International Union of Materials Research Societies – International Conference on Electronic Materials 2010 (IUMRS-ICEM 2010), 2010.08.22, KINTEX, Goyang,

Korea.

Domestic conference:

- 1) 석철균, 박환열, 최대한, 임원철, 송중환, 박용조, 송진동, 윤의준 “Be 임플란트된 InSb 기관의 열처리를 통한 결함 회복 및 활성화 연구”, 2014 한국군사과학기술학회 종합무기학술대회, 2014.06.20, 국제컨벤션센터, 제주.
- 2) 박세훈, 최대한, 박환열, 석철균, 박용조, 윤의준, “유도결합 플라즈마 화학 기상 증착법(ICP-CVD) 을 이용한 Si₃N₄ 박막 증착 연구”, 2014 한국군사과학기술학회 종합무기학술대회, 2014.06.19, 국제컨벤션센터, 제주.
- 3) 석철균, 최대한, 이재열, 김수진, 박세훈, 박환열, 박용조, 윤의준 “적외선 검출기용 InSb FPA 표면에 형성되는 Passivation 층의 열화 및 이에 의한 특성 파괴 메커니즘 연구”, 2014 한국군사과학기술학회 종합무기학술대회, 2014.06.19, 국제컨벤션센터, 제주.
- 4) 정진욱, 박세훈, 석철균, 박용조, X. Chen, J. Shao, 윤의준,

“Unusual photoluminescence peak shift of InSb epitaxial layers grown by LP-MOCVD”, 한국반도체학술대회, 2014.02.24, 한양대학교, 서울.

- 5) 석철균, 최민경, 정진욱, 박세훈, 박용조, 양인상, 윤의준, “Effects of surface damage on Raman spectrum of etched InSb(100) surface”, 한국반도체학술대회, 2014.02.24, 한양대학교, 서울.
- 6) 석철균, 최민경, 정진욱, 박세훈, 박용조, 양인상, 윤의준, “Effect of annealing under antimony ambient on structural recovery of plasma-damaged InSb (100) surface”, 한국진공학회 동계학술대회, 2014.02.11, 휘닉스파크, 평창.
- 7) 석철균, 정진욱, 박세훈, 박용조, 윤의준, “고성능 중적외선 검출소자 제작을 위한 InSb 플라즈마 식각 방법 비교 연구”, 국방기술학술대회, 2013.07.03, 고려대학교, 서울,
- 8) 정진욱, 박세훈, 석철균, 박용조, 윤의준, “유기화학기상증착법을 이용한 고품질의 InSb 에피성장

연구”, 국방기술학술대회, 2013.07.03, 고려대학교, 서울.

- 9) 석철균, 박세훈, 정진욱, 박용조, 윤의준, “고성능 중적외선 검출소자 제작을 위한 InSb 플라즈마 식각 방법 비교 연구”, 한국군사과학기술학회 종합무기학술대회, 2013.07.03, 국제컨벤션센터, 제주.
- 10) 정진욱, 박세훈, 석철균, 윤의준, “유기화학기상증착법을 이용한 InSb 동종 에피성장 연구”, 한국군사과학기술학회 종합무기학술대회, 2013.07.03, 국제컨벤션센터, 제주.
- 11) 박세훈, 정진욱, 석철균, 신상훈, 송진동, 박용조, 윤의준, “p-type doping study for InSb grown by metalorganic chemical vapor deposition”, 한국군사과학기술학회 종합무기학술대회, 2013.07.03, 국제컨벤션센터, 제주.
- 12) 정진욱, 박세훈, 석철균, 여환국, 윤의준, “Homo-epitaxial growth of InSb by MOCVD”, 한국광전자학회, 2012.11.16, 서울.
- 13) 박세훈, 김수진, 석철균, 박진섭, 윤의준, “The origin of interface states in Si₃N₄/InSb and SiO₂/InSb structures for

MWIR photodetectors”, 한국반도체학술대회, 2011.02.18,
국제컨벤션센터, 제주.

- 14) 김수진, 박세훈, 이재열, 석철균, 박진섭, 윤의준, “InSb 적외선 소자제작을 위한 SiO₂, Si₃N₄ 증착 온도에 따른 계면 특성 연구”, 한국진공학회 동계학술대회, 2011.02.11, 휘닉스파크, 평창.
- 15) 박세훈, 이재열, 김정섭, 김수진, 석철균, 양창재, 박진섭, 윤의준, “InSb 적외선 감지 소자용 Si₃N₄, SiO₂ 절연막 계면 특성 연구”, 한국진공학회 하계학술대회, 2010.08.18, 비체펠리스, 보령.
- 16) 이재열, 박세훈, 김정섭, 양창재, 김수진, 석철균, 박진섭, 윤의준, “Quantitative analysis of formation of oxide phases between SiO₂ and InSb”, 한국진공학회 하계학술대회, 2010.08.18, 비체펠리스, 보령.

Patent

- 1) 석철균, 윤의준, 김치연, “인듐안티모나이드의 플라즈마

다중 식각 방법 및 이에 의한 인듐안티모나이트 기판”,
대한민국, 출원번호: 10-2014-0026516, (2014).

2) 석철균, 윤의준, 박용조, “플라즈몬 구조를 이용한
수광소자 및 그 제조 방법”, 대한민국, 출원중 (2014).

17) **Chulkyun Seok**, Yongjo Park, Euijoon Yoon, “Plasmonic device
with photonic crystal and its fabrication method”, U.S.A, in
preparation (2014).

Award

1) “재료조직사진상 학술부문 가작상”, 대한금속재료학회
주관, Apr. 24th, 2014.

2) “Best Poster Award” at the Nano Korea 2014, Jul. 4th, 2014.